

XFEL/SPring-8  
Beamline Technical Design Report  
Ver. 2.0

February, 2010

SPring-8 Joint Project for XFEL

Experimental Facility Group

## **Preface**

In 2010, construction of the X-ray Free Electron Laser (XFEL) facility entered the last year of its 5-year plan. The XFEL is one of Japan's "key technologies of national importance" as specified in the 3rd Science and Technology Basic Plan. As is customary with this kind of construction, the project has taken steps towards downstream from upstream. Light sources, beamlines, experimental devices and relevant utilities which lie downstream from the Accelerator finally began to construct.

At the XFEL Project Head Office, the concept designs for the beamlines and experimental devices have been led mainly by the Experimental Facility Group. The Project Head Office is responsible for compiling the achievements and disclosing them in a design report with the intention of improving the facility by obtaining extensive feedback from affiliate researchers.

Under this policy, we are now publishing the design report. However, we are still in process of finalizing some details. On another front, we need to continue with order placement during this fiscal year. Therefore, we intend to hear from a broad range of interested people as early as possible in order to incorporate their views into future plans.

With great appreciation for all of your past support, we look forward to your continued collaboration and opinions on the XFEL facility construction plan.

February, 2010  
XFEL Project Head Office  
Experimental Facility Group  
Group Director  
Tetsuya Ishikawa

## **Authors**

### **RIKEN-JASRI XFEL Project Head Office**

Shunji Goto, Takaki Hatsui, Atsushi Higashiya, Hiroaki Kimura, Togo Kudo, Mitsuru Nagasono, Yoshinori Nishino, Haruhiko Ohashi, Kenji Tamasaku, Yoshihito Tanaka, Tadashi Togashi, Hiromitsu Tomizawa, Kensuke Tono, and Makina Yabashi  
(Experimental Facility Group)

Sunao Takahashi  
(Accelerator Construction Group)

Toru Hara, Hitoshi Tanaka, Takashi Tanaka, and Kazuaki Togawa  
(Accelerator Construction Group)

Yukito Furukawa, Tomohiro Matsushita, and Toru Ohata  
(Control System Group)

Yoshihiro Asano and Toshiro Itoga  
(Safety Design Group)

## **Editor**

Makina Yabashi (Experimental Facility Group/ Beamline Construction Team, Team leader)  
Tetsuya Ishikawa (Experimental Facility Group, Group director)

## **Publication**

RIKEN JASRI XFEL Project Head Office, Experimental Facility Group  
1-1-1, Kouto, Sayo-cho, Sayo, Hyogo, 679-5148  
e-mail: [xfeluser@spring8.or.jp](mailto:xfeluser@spring8.or.jp)

## **Publication Date**

Japanese:First Edition: June 17, 2008  
English :First Edition: February 22, 2010  
\*all rights reserved

## Contents

1. Summary	1
2. Light Source Properties	3
2-1. Outline	3
2-2. Electron Beam Parameters	3
2-3. Undulator Parameters	6
2-4. FEL Radiation Parameters	7
2-5. Spontaneous Radiation	14
3. Guidelines for Beamline Design	15
3-1. Outline	15
3-2. Configuration Plan	15
3-3. Optical System	15
3-4. Optical Elements	17
3-5. Monitor	18
3-6. Radiation Shielding	18
4. Beamline Configuration and Specifications of Components	19
4-1. Outline	19
4-2. Beamline Arrangement and Shielding Hatches	19
4-3. Front-end (FE)	21
4-4. Beamline Optics and Transport-Channel	24
5. Data Acquisition System (DAQ)	36
5-1. Data Acquisition System (DAQ)	36
5-2. X-Ray 2-D Detectors	42
6. Civil Engineering: Experimental Facility	47
6-1. Outline	47
6-2. Experimental Hall	47
6-3. Experimental Preparation Room	48
6-4. Sample Preparation Room	48
6-5. Carry-in Room	48
6-6. Noise Shielding	48
APPENDIX	52
A1. Dose Estimation for XFEL	52
A2. Estimation of Transmissivity	63
A3. Estimation of Scattering Power	71
A4. Revision Record	72

## 1. Summary

The X-ray Free Electron laser (XFEL) is a new x-ray source distinguished by the high-brightness, high-coherence and short-pulse of the light generated. XFEL facilities are under development in the US, Europe and Japan [1-1, 1-2, and 1-3]. The XFEL Project Head Office organized by RIKEN and JASRI is managing the 5-year construction plan, running from 2006 to 2010, at the Japan's XFEL SPring-8 campus. The XFEL is composed of an accelerator for generating a electron beam, undulators for producing XFEL radiation, and beamlines for tailoring XFEL radiation for user experiments. This report presents a design of the beamline with performance data of the light source, information which are most important for user experiments.

Historically, advances of synchrotron light sources have stimulated to develop new beamline technologies. The era of the second-generation synchrotron light source with dedicated storage rings occurred in the 1970s and 1980s. This period saw the significant development of x-ray monochromators for quick scan of wavelength with high stability, as well as the adaptation of ultrahigh vacuum systems for connecting beamlines to storage rings. The era of the third-generation synchrotron light sources, which combines low-emittance storage rings with undulators, began in the 1990s. The greatest challenge was to develop an optical system for managing high heat loads from an undulator. Now, the key criteria imposed on XFEL beamlines are “coherence” and “pulse”, which require speckle-free optical systems that do not degrade coherent wavefronts, and development of beam handling/detection systems that enable efficient use of isolated high-intensity X-ray pulses. To achieve these criteria, the XFEL Experimental facility Group led analyses from various perspectives, this report summarizes the results of those discussions and considerations.

The XFEL facility at SPring-8 will have the capacity to contain 5 beamlines. The first-period construction plan which completes in 2010 includes two beamlines, an FEL beamline of the hard X-ray region (BL3), which is a main target of this report, and a broadband beamline (BL1), which will be presented in the near future.

This document is organized as follows: Chapter 2 summarizes the performance of the light source. Chapter 3 presents fundamental guidelines for the design of beamlines, and based on this Chapter, Chapters 4 presents the configuration of beamlines and specifications for each component. Chapter 5 provides specifications for the data acquisition system and the two-dimensional detector required for this purpose. Chapter 6 presents a description of the civil engineering including the experimental building. Finally, the Appendix includes information on several independent themes.

## References

- [1-1] T. Tanaka, & T. Shintake, (Eds) SCSS X-FEL Conceptual Design Report, (RIKEN Harima Institute, Hyogo, Japan, 2005).
- [1-2] J. Arthur et al., “Linac Coherent Light Source (LCLS) Conceptual Design Report”, SLAC-R593 (Stanford, 2002).
- [1-3] M. Altarelli et al. (Eds) XFEL: The European X-Ray Free-Electron Laser, Technical Design Report. Preprint DESY 2006-097, (DESY Hamburg, 2006).

## 2. Light Source Properties

### 2-1. Outline

This chapter describes XFEL radiation properties with accelerator parameters for the SPring-8 XFEL project.

Our accelerator system uses a thermionic electron gun and a multistage bunch compression system for generating an electron beam with high density and low emittance. Although this system, as well as our variable-gap undulators, provide large flexibility for radiation properties, we here summarize results for typical parameter sets at a electron beam energy  $E_B = 8$  GeV. Note that this chapter treats only single-bunch operation, although the choke-mode C-band accelerating tubes allow us to perform multi-bunch operations (40 pulse train at a maximum with 4-ns interval),.

### 2-2. Electron Beam Parameters

The electron beam parameters are summarized in Table 2-2-1. The time dependencies between peak current and normalized emittance, energy spread and averaged beam energy are depicted in [Fig.2-2-1](#), [Fig.2-2-2](#) and [Fig.2-2-3](#), respectively. Simulations were conducted in combination with a one-dimension PIC code, PARMELA, and ELEGANT.

Table 2-2-1 Electron Beam Parameter

Beam energy (GeV)	8
Peak current (kA)	4.4
Slice emittance	0.77
Slice energy spread	7.1e-5
Total charge (nC)	0.29
Bunch width (fs, FWHM)	55
Beam size at ID exit (um, rms)	35
Repetition rate (Hz)	60 (max) to 1 (min)

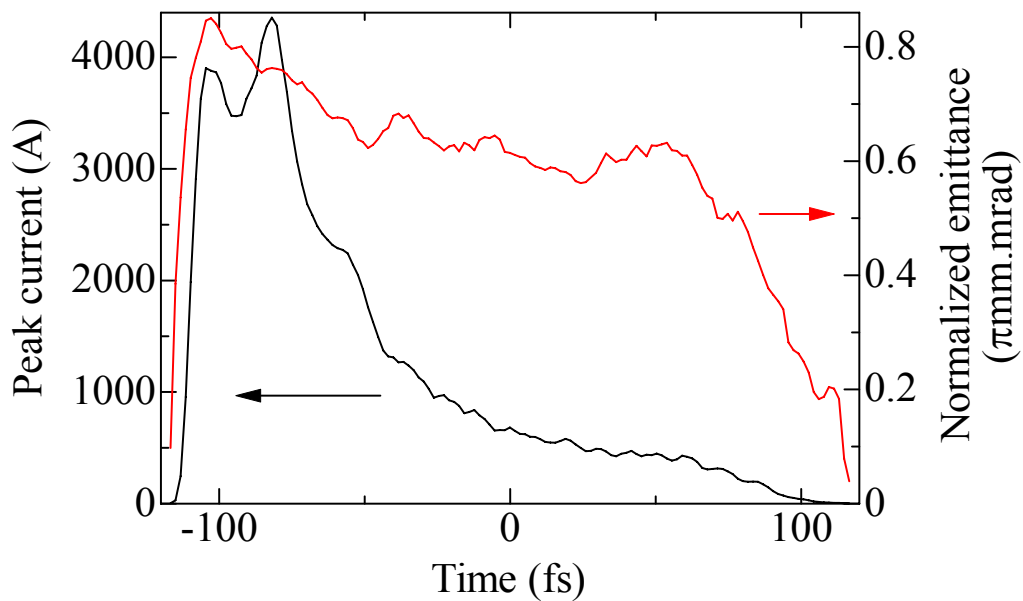


Fig.2-2-1 Time dependences of peak current (left axis) and normalized emittance (right axis)

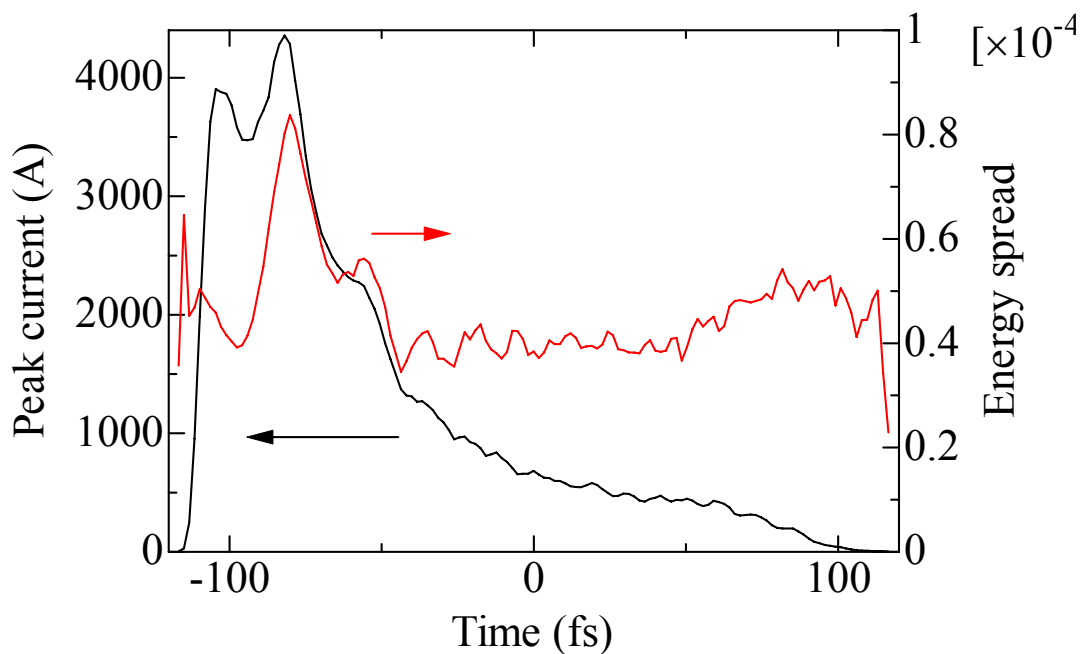


Fig.2-2-2 Time dependences of peak current (left axis) and energy spread (right axis)

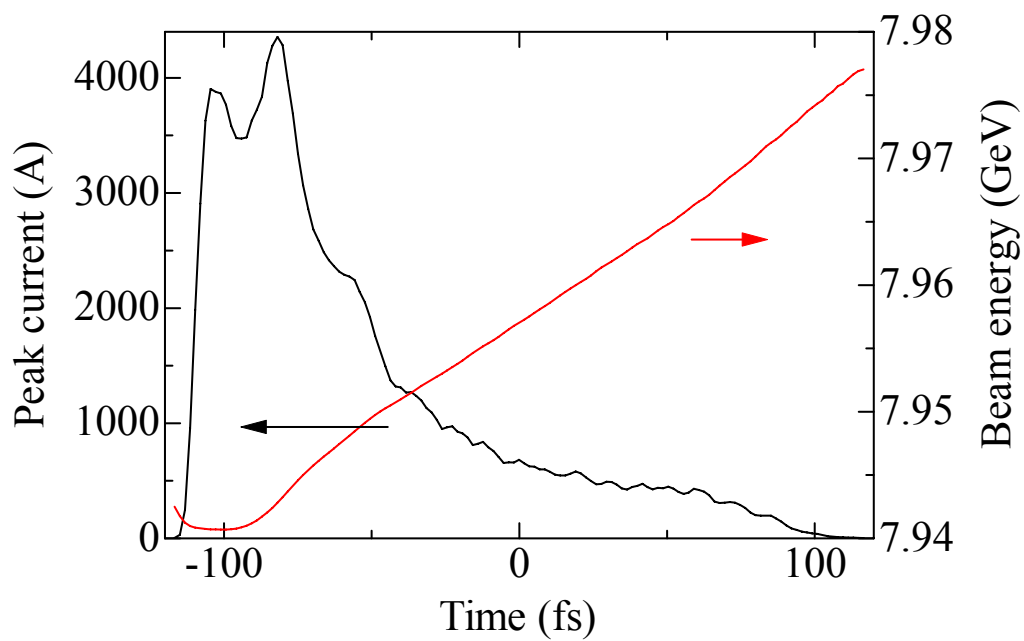


Fig.2-2-3 Time dependences of peak current (left axis) and averaged beam energy (right axis)

### 2-3. Undulator Parameters

The undulator parameters for BL3 are summarized in [Table 2-3- 1](#)

[Table 2-3-1](#) Undulator Parameter for BL3

Periodic length, $\lambda_U$ (mm)	18
Segment length (m)	5
Number of segments	18
Total periodic number	5000
Maximum deflection parameter, $K^{\ast 1}$	2.3
Average betatron function, $\beta_x / \beta_y$ (m)	25 / 25

$$\ast 1: K = \frac{eB_0\lambda_U}{2\pi m_e c}, B_0: \text{Peak magnetic field}$$

## 2-4. FEL Radiation Parameters

We conducted simulations of FEL radiation parameters using a code SIMPLEX [2-1]. Various parameters set at a fixed  $K$ -value of 2.2 are summarized in Table 2-4-1. In Fig.2-4-1, dependences of peak power and pulse energy on photon energy are calculated for  $K$ -values of 2.2, 1.9, 1.5, and 1.1. For larger  $K$ -values the photon energy decreases (i.e., the wavelength increases) from Eq. 2-4-3. At the same time, peak power enhances because of increased FEL parameter  $\rho$  from Eq. 2-4-1. We also show the gain curve along the undulator with higher  $K$ -values in Fig.2-4-2. For larger  $K$ , the pulse energy reaches saturation more quickly due to smaller gain lengths from Eq. 2-4-2.

Typical time and energy spectrum are shown in Fig. 2-4-3 and Fig. 2-4-4, respectively. The correlation plot between time and energy is presented in Fig. 2-4-5.

Table 2-4-1 FEL radiation parameters (fundamental radiation)

Electron beam energy (GeV)	8
Repetition rate (Hz)	60 (max) to 1 (min)
UND K value	2.2
FEL parameter ※2	4.4e-4
Saturation length (m) ※3	45
Wavelength (nm) ※4	0.13
Photon energy (keV)	9.9
Bandwidth	9.2e-4
Source size (um, rms)	33
Angular divergence (urad, rms)	0.73
Peak power (GW)	29
Pulse energy (mJ)	0.78
Photons per pulse (phs/pls)	5.0e11
Pulse width (fs, FWHM)	30
Power ratio of higher-order harmonic (2nd:1st)	1.3e-4
Power ratio of higher-order harmonic (3rd:1st)	2.8e-3

$$\text{※2: } \rho = \left[ \frac{\gamma \lambda^2 r_e n_e}{8\pi} F_1(K) \right]^{\frac{1}{3}} = \left[ \frac{\gamma^2 \lambda^2 r_e I_p}{16\pi^2 c e \beta \varepsilon_n} F_1(K) \right]^{\frac{1}{3}} \quad (\text{Eq. 2-4-1})$$

$$F_1(K) = \frac{K^2}{(1 + K^2/2)^2} \left[ J_0 \left( \frac{K^2/4}{1 + K^2/2} \right) - J_1 \left( \frac{K^2/4}{1 + K^2/2} \right) \right]^2$$

$$\gamma = E_B / m_e c^2 : \text{Lorentz factor}$$

$$\lambda: \text{Radiation wavelength}$$

$n_e$ : Density of the e-beam

$I_p$ : Peak current of the e-beam

$\varepsilon_n$ : Normalized emittance of the e-beam

$\beta$ : Average betatron function

$$\text{※3: } L_g = \frac{\lambda_U}{4\pi\sqrt{3}\rho} \quad (\text{Eq. 2-4-2})$$

$$\text{※4: } \lambda = \frac{\lambda_U}{2n\gamma^2} \left( 1 + \frac{K^2}{2} \right) \quad (\text{Eq. 2-4-3})$$

$n$ : Order of harmonic

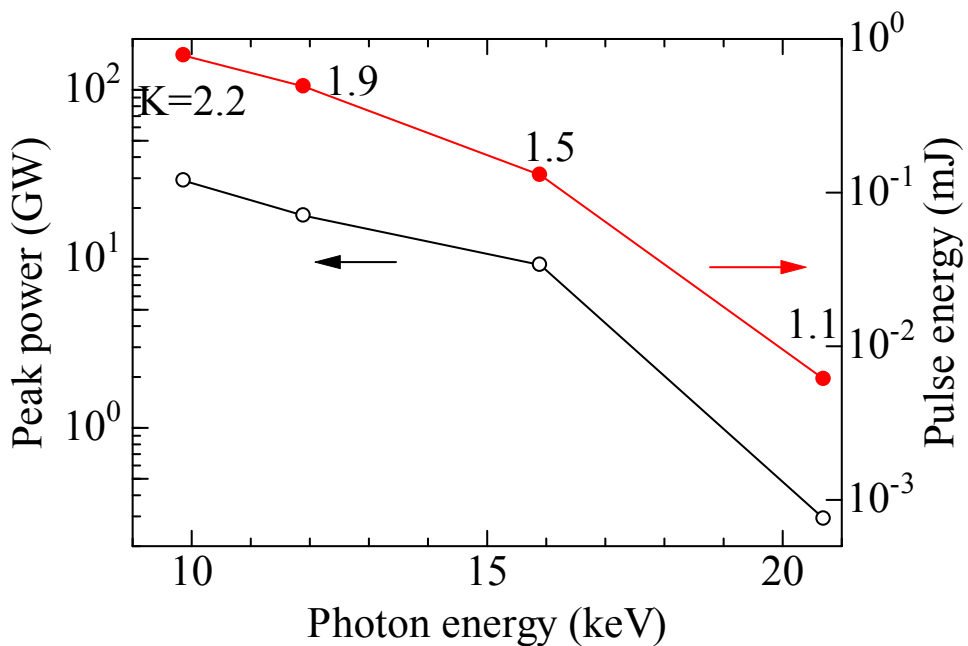


Fig. 2-4-1 Dependences of peak power (left axis) and pulse energy (right axis) on photon energy for  $K=2.2, 1.9, 1.5, 1.1$ .

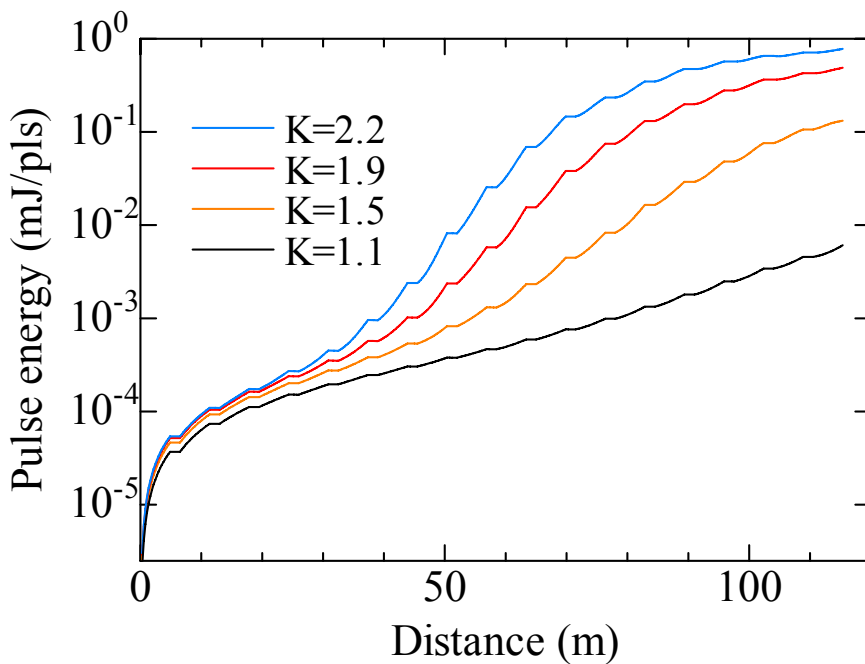


Fig.2-4-2 Gain curve along undulator with  $K=2.2, 1.9, 1.5, 1.1$ .

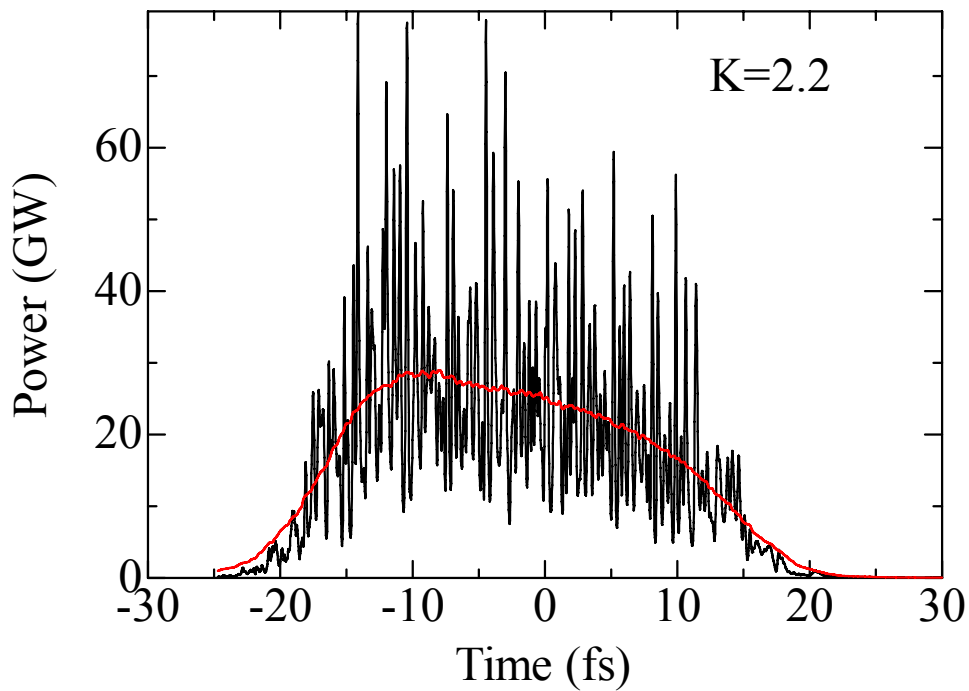
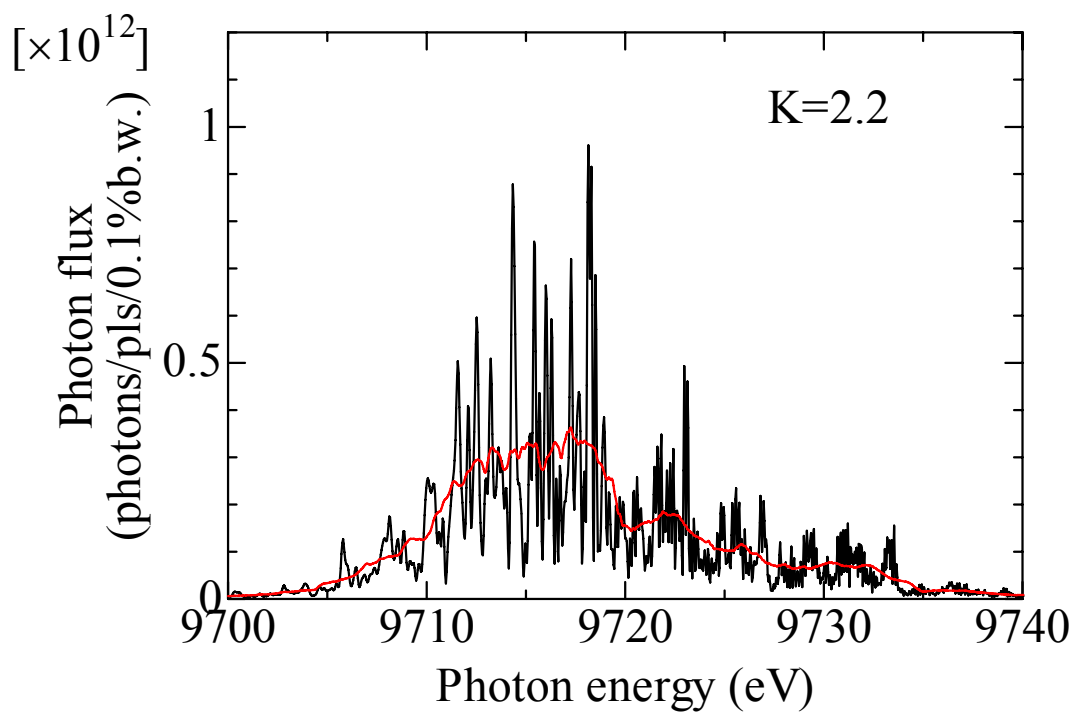
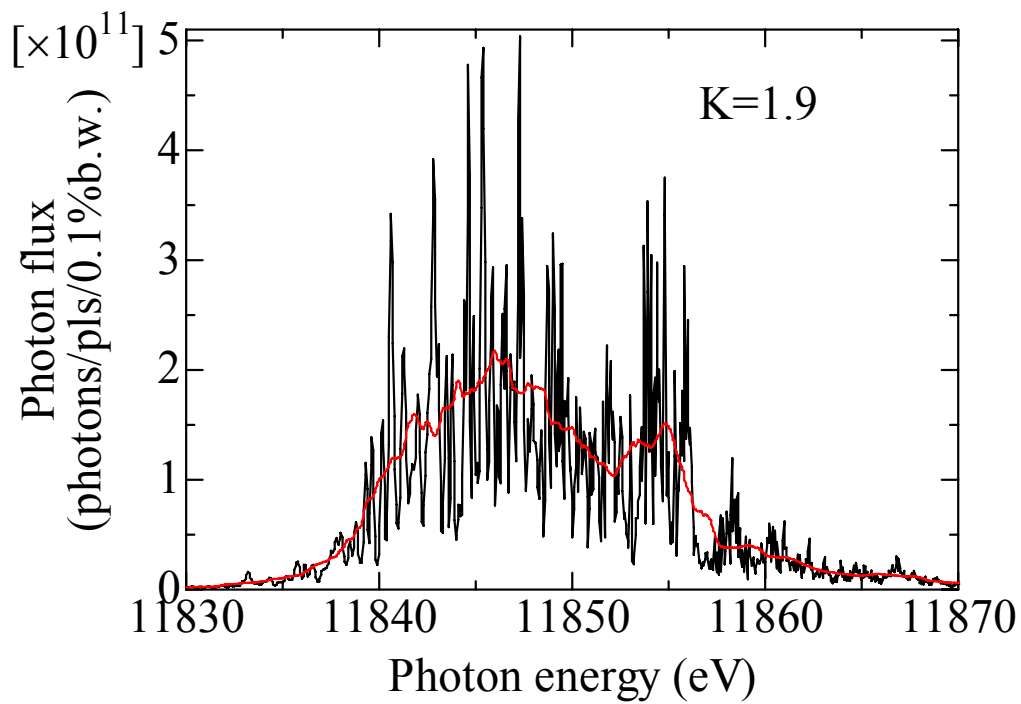


Fig. 2-4-3 Time spectrum at  $K=2.2$ .

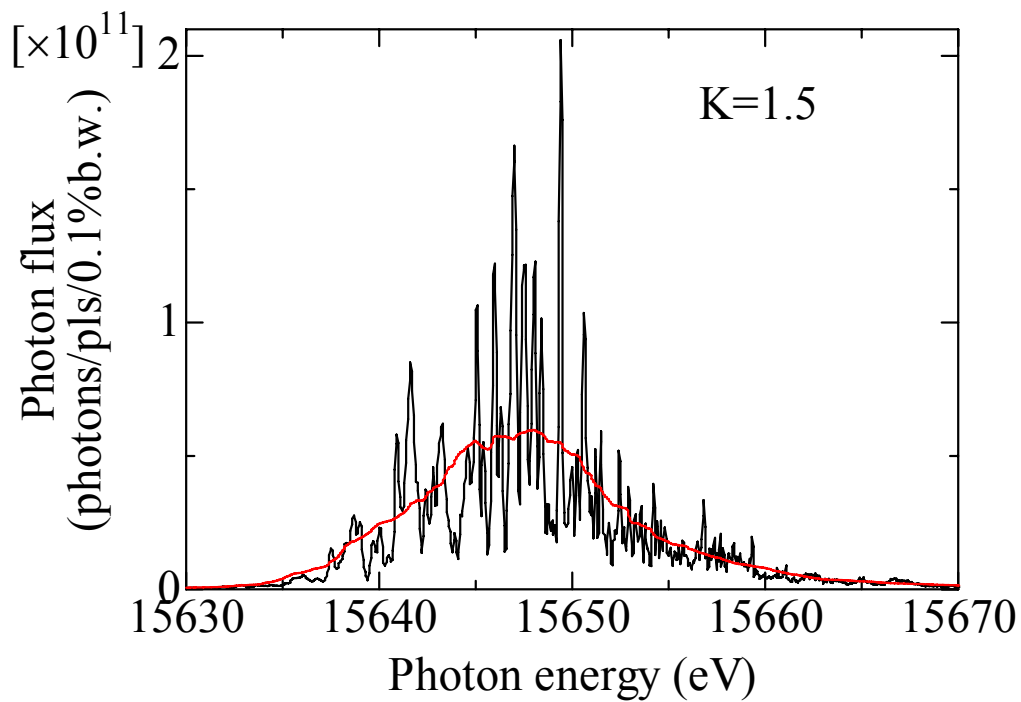
(a)



(b)



(c)



(d)

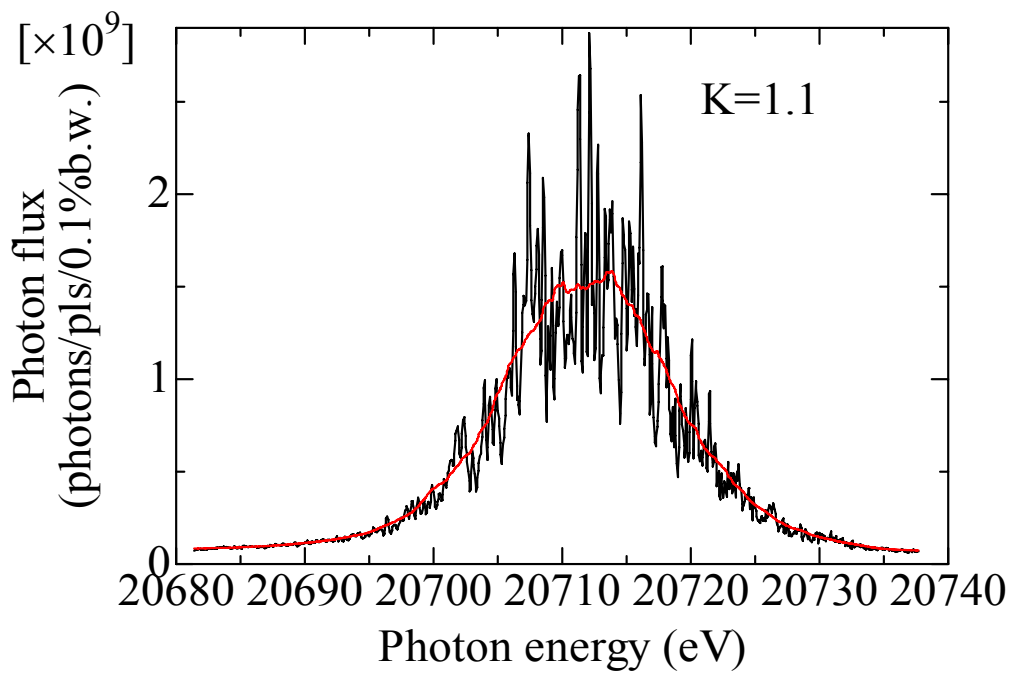


Fig. 2-4-4 Energy spectrum for (a)K=2.2, (b) 1.9, (c) 1.5 , and (d) 1.1.

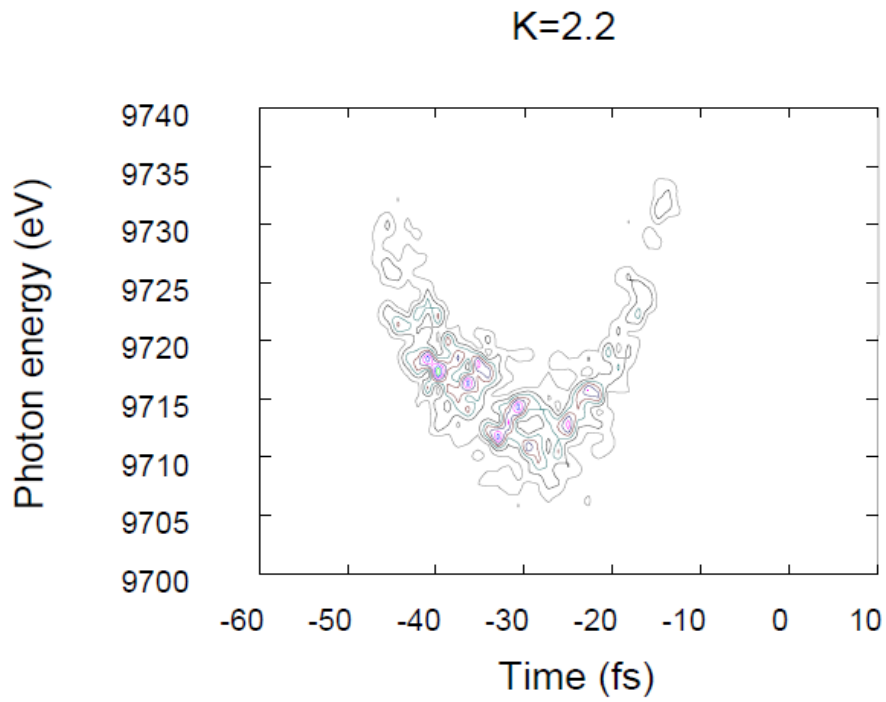


Fig.2-4-5 Correlation plot between photon energy and time at  $K=2.2$ .

## 2-5. Spontaneous Radiation

Spontaneous radiation parameters are summarized in [Table 2-5-1](#).

[Table 2-5-1](#) Spontaneous radiation parameters

Beam energy (GeV)	8
Max. total charge (nC)	1.5
Max. repetition rate (Hz)	60
UND K value	2.2
Average power (W)	0.57
Power divergence H/V (urad, rms)	71/43
Power density at $L=64$ m (distance from UND exit) ( $\text{mW}/\text{mm}^2$ )	$1.5^{\ast 1}$
Partial power after $\phi 10$ mm aperture at $L=64$ m (mW)	117

※1 Computed the center of the undulator as a virtual light source

## References

[2-1] Takashi Tanaka, “FEL simulation code for undulator performance estimation”, *Proc. 2004 FEL conf.*, 435-438 (2004), <http://radiant.harima.riken.go.jp/simplex>.

### 3. Guidelines for Beamline Design

#### 3-1. Outline

XFEL is a new light source which has significant differences from conventional synchrotron sources. In designing beamlines, it is necessary to introduce new considerations for fully exploiting the beam characteristics such as perfect transverse coherence, ultrahigh brightness, and femtosecond pulse duration.

In 2007, the Experimental Facility Group of the Joint Project Team developed a discussion for setting basic guidelines, prior to the detailed design works. This chapter summarizes essential policies given at the considerations.

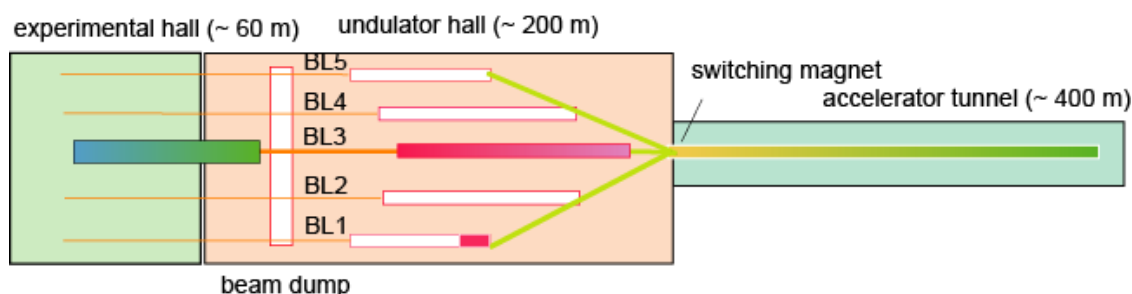


Fig. 3-1-1 Schematic of Machine Layout

#### 3-2. Configuration Plan

The Joint-Project Team designed the Undulator Hall to be capable of eventually supporting 5 beamlines, they are aligned in parallel with a separation of 3 m. These beamlines are branched from a switching magnet that selects and transports the electron beam. The maximum lengths of the undulators to be installed are about 80 m (BL1 and BL5), 120 m (BL2 and BL4) and 150 m (BL3), respectively. The three beamlines in the middle (BL2, BL3, BL4), which can contain a larger number of undulator segments, are planned to be dedicated for hard x-ray FEL regime, while the remaining (BL1, BL5) are for soft x-ray or extreme ultraviolet (EUV) regimes. In the initial phase of the construction plan scheduled to complete in 2010, BL3 is constructed as a hard X-ray FEL beamline. Additionally, BL1 is arranged as a “broadband beamline” which covers a longer wavelength regime (Fig. 3-1-1)

The 3-m separations between the contiguous beamlines are rather small compared to typical values in conventional beamlines at storage rings. Since we found that it is difficult and inefficient to build shielding hutches independently for each beamline, some of hutches contain plural beamlines. In this case, special care should be paid for reduce interferences between beamlines in the operation phase.

#### 3-3. Optical System

## (1) Wavelength range

A linac-based light source is able to change electron beam energy without serious difficulties. For BL3 undulators with a periodic length of 18 mm, the lowest photon energy is about 10 keV with an electron beam energy of  $E_B=8$  GeV, while soft x-rays with a photon energy of 2.5 keV can be generated with  $E_B=4$  GeV operation. Although BL3 is dedicated mainly for hard x-ray utilization, the extension to the soft x-ray region expands availability. For this purpose, Beryllium windows, are used for separating vacuum sections at the hard x-rays beamlines, and are designed to be retractable from the optical axis. In this case, differential pumping systems are used for keeping vacuum separation.

For the main optical components, total reflection mirrors (< 15 keV) and a double-crystal monochromator (DCM, 4-30 keV with Si 111) are prepared. The former are used to transport soft x-rays to the experimental hutches.(Fig. 3-4-1)

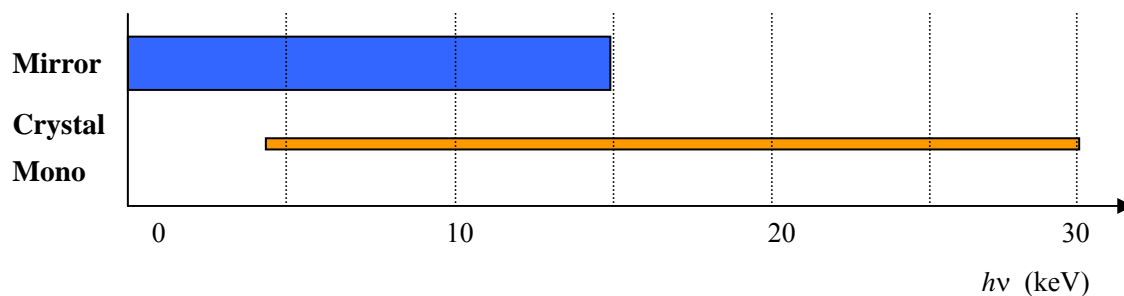


Fig. 3-4-1 Optical Energy Range covered by Optical System

## (2) Bandwidth

The bandwidth of XFEL is expected to be  $\sim 0.1\%$ , as seen in Sect. 2. Total reflection mirrors work as a low-pass filter and transport XFEL to experimental hutches without a reduction of bandwidth. The DCM works as a band-pass filter with a bandwidth of  $0.01\%$  with Si 111 reflection. The former is employed for experiments that require higher photon flux, while the latter is used for applications that need an accurate control of wavelength.

## (3) Harmonic Reduction

FEL radiation contains higher harmonic components with intensities of  $0.1\%$  and  $1\%$  for second and third harmonics, respectively, compared to the fundamental radiation. Double mirrors are used for reduction of component for more than a few orders of magnitude. Two sets of mirrors are prepared for switching cutoff energies. The first mirror is commonly used, while the second mirrors (2a, 2b) are switched for each energy. For DCM, the reduction ratio to the fundamental radiation is less than  $1\%$  and  $10\%$  for 2nd and 3rd harmonics, respectively.

## (4) Fixed-Exit Optical Axis

It is desirable to keep the optical axes of XFEL radiation to be constant, even when, one changes

the optical devices or alters the photon energy. A fixed-exit design is applied for the DCM, while a pair of mirrors is employed for the mirror system. The offset between the incident and exit beams are kept constant for both DCM and the mirrors, the DCM and the mirrors are exclusively employed. The offset value is determined to be 20mm, by considering the capability for  $\gamma$ -ray shielding and a moderate distance between mirrors. Note that this value is smaller than the offset (30 mm) of a standard X-ray beamline at SPring-8. The beam is vertically deflected in order to prevent loss of diffraction efficiency for DCM (note that FEL is horizontally polarized).

#### (5) Stability

The beam divergence of the XFEL is approximately 1 urad, which requires extremely high stability for the optics. A basic strategy for designing the mechanisms of the optical devices is to increase rigidity, to reduce the number of axes, and to limit the movable range, the temperature should be highly stabilized. Ion pumps, rather than a combination of scroll and turbo-molecular pumps, are used for vacuum pumps in normal operation to avoid vibration.

#### (6) Attenuator

Attenuators required to reduce XFEL intensity for experimental reasons and for alignment purpose. The transmittance is controlled from 100% to 0.1% with combining attenuators of solid and gas. Intentional detuning of undulators might be used for further reduction of intensity.

### 3-4. Optical Elements

#### (1) Reduction of speckles

XFEL with high spatial coherence requires extremely high quality (surface-figure accuracy and density homogeneity) for optical elements. After R&Ds at SPring-8, speckle-free quality have been achieved for total-reflection mirrors and Be-windows. For monochromator crystals, silicon satisfies the speckle-free quality, while continuative R&D is required for achieving speckle-free diamond crystals.

#### (2) Resistivity to high pulse energy

XFEL pulse deposits a high energy within a short time onto optical elements through absorption processes. Light elements are preferred to avoid melting or ablation. An absorber of light elements are attached in front of metal materials used for shutters or slits.

#### (3) Vacuum environment

The optical elements are used within ultrahigh-vacuum and oil-free condition in order to avoid contamination of particles, which can cause serious radiation damage, to optical elements.

#### (4) Cooling requirement

It is estimated that the average powers in spontaneous emission and FEL radiation are 0.6 W and below 60 mW, respectively, [ $10^{12}$  photons/pls (@10 keV)  $\rightarrow$  1 mJ/pls  $\rightarrow$  60 mW] with a single-bunch operation at a repetition rate of 60 Hz. The former component is further reduced to below 0.12W with the first collimator ( $\phi$ 10 mm @64 m from ID2 exit) in the front-end section. An indirect water-cooled system is adopted for cooling of the optical elements. Note that the average power of the monochromatic X-ray of SPring-8 BL19LXU is about 0.1W. Reconsideration is required for multi-bunch operation that has a power 40 times greater.

### 3-5. Monitor

#### (1) Shot-to-shot measurement

Since SASE-FEL starts up from noise, radiation properties such as energy and temporal spectra change in shot-to-shot. For conducting reliable experiments, it is desired to monitor these properties in every shot (60 Hz) with a non-destructive method. For commissioning of tuning, we can apply a destructive-typed monitor with a repetition rate of 1 Hz.

#### (2) Commissioning

When commissioning, monitors and optics which directly observe the optical axis of the  $\gamma$ -ray may be temporally required, extra space is prepared upstream of the  $\gamma$ -stopper.

### 3-6. Radiation Shielding

The XFEL beamline is settled at a location downstream to the 8-GeV linac. Here, a rate of  $\gamma$ -rays in radiation is supposed to be higher than those for SPring-8 beamlines at the 8-GeV storage ring. It is required for reducing these unwanted contaminations at the front-end section in the Undulator Hall. The off-axis contaminations are removed with a double collimator at the front-end section. The separation of on-axis contaminations from XFEL are realized with optical components. Note that these components as “first scatters” should be regarded as a neutron sources from a viewpoint of radiation safety, because the photonuclear reaction converts  $\gamma$ -rays to neutrons when interacted with matters. For shielding neutrons and  $\gamma$ -rays, the optics hutch containing the “first scatters” is made of concrete with a thickness of 80 cm or larger

## 4. Beamline Configuration and Specifications of Components

### 4-1. Outline

This chapter presents the more detailed configuration of the beamline and specifications of the components, which are designed based on the concepts from the previous chapter.

### 4-2. Beamline Arrangement and Shielding Hutches

Fig. 4-2-1 shows the arrangement of five beamlines in the experimental hall. Optics hutches and experimental hutches are set up to allow storage of two or more beamlines due to the limited distance (~3 m) between the adjoining beamlines.

The optical hutches are grouped into OH1 (BL1-2) and OH2 (BL3-5). Thus it will be possible to renew a beamline of one group while operating a beamline from another group. The lengths of the optical hutches (the inner size of 17m along the optical axis) are determined based on the beamline configuration of BL3.

The four experimental hutches are set in tandem. The dimensions are summarized in Table 4-2-1. Each hutch has sliding doors for equipment entrance, cable ducts, and a movable X-ray stopper, downstream at the end. Electric power, coolant water, and compressed air are supplied for every hutch. The beam height in these hutches are 1420 mm, which include an offset value of 20 mm after the beamline optics in the optics hutch.

The initial phase, all four hutches will serve, BL3., when BL2 and BL4 are allocated, some of these hutches will be assigned to these beamlines. Therefore it will be possible to perform experiment with multiple beamlines operating at the same time. Fig. 4-2-2 illustrates one example. EH1 and EH2 belonging to BL4, while EH3 and EH4 are used for BL3 by utilizing shielded beam pipes. BL2 and other beamlines are transported to an experimental hall of the SPring-8 storage ring.

BL1 and BL5 are supposed to work as soft X-ray or EUV beamlines, which do not require experimental hutches due to their small penetration powers. The axes of these beamlines are deflected in the horizontal direction by using optics in the optical hutches, to prevent interference with BL2 and BL4.

Table 4-2-1 Parameters for the Experimental Hutches

Hutch	Size L×W×H (m)	Size of Equipment Entrance W×H (m)
EH1	6×7×4	2.5×3
EH2	7×7×4	2.5×3
EH3	7×7×4	3×3
EH4	9×7×5	4×3

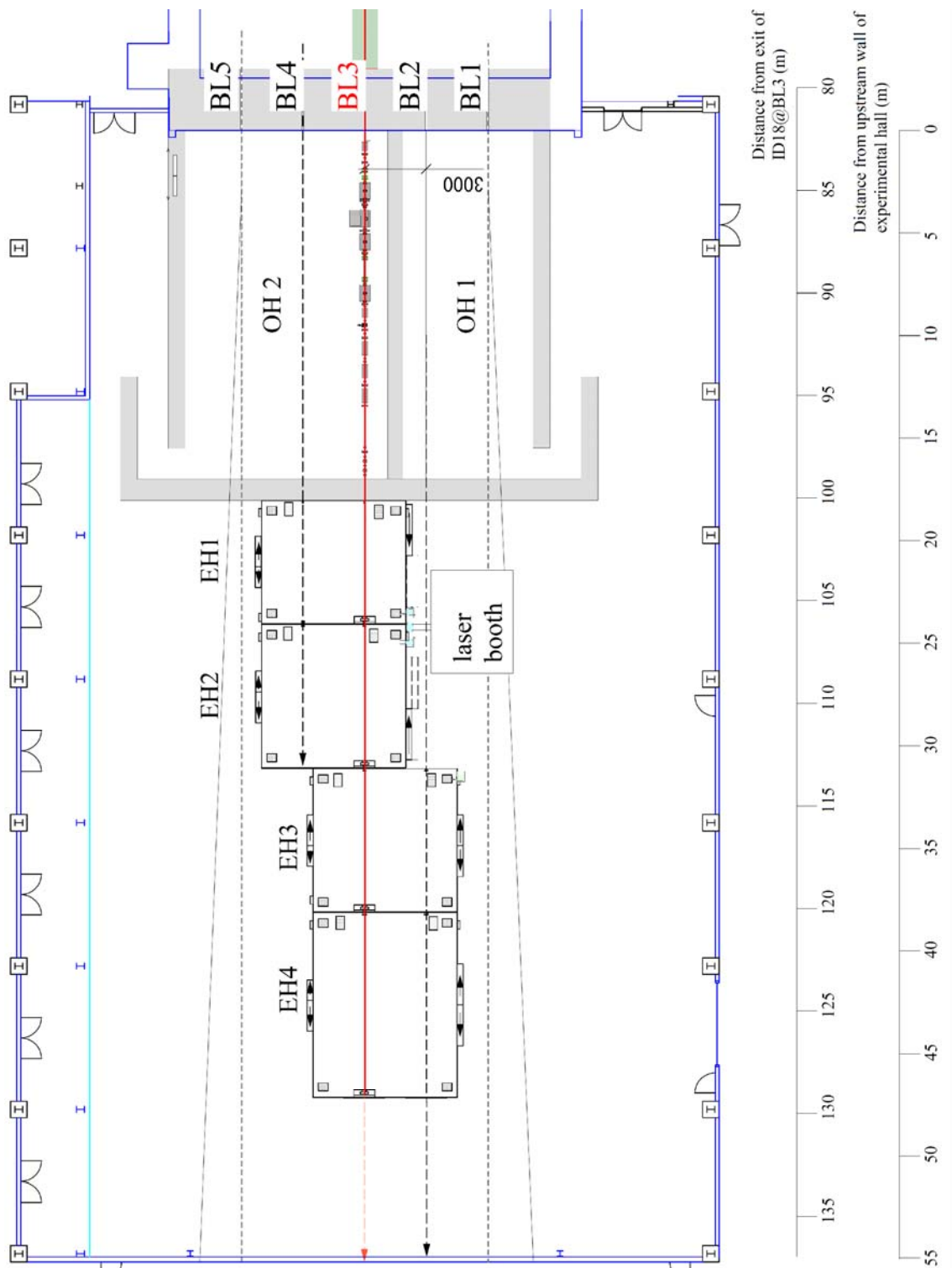


Fig. 4-2-1 Plan of beamline configurations in the experimental hall

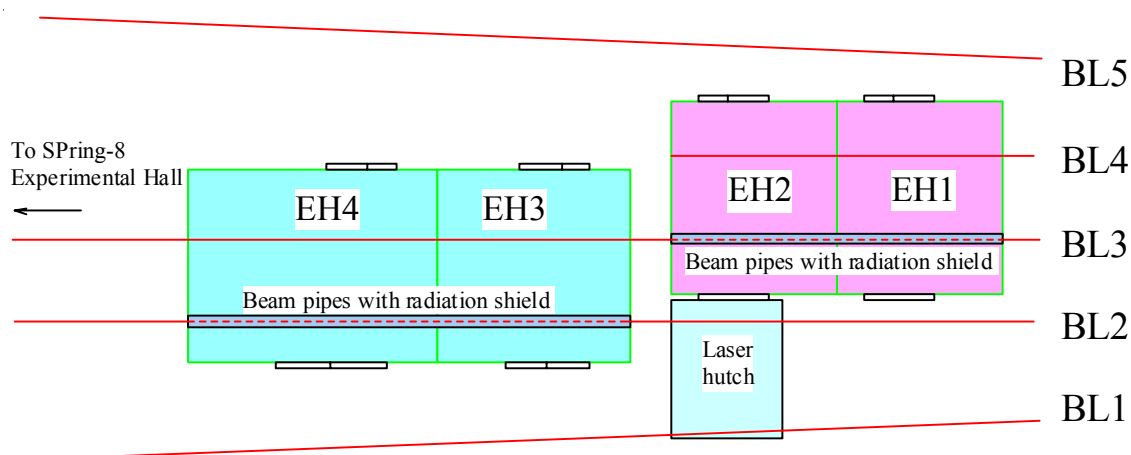


Fig. 4-2-2 Beamline operation plan

### 4-3. Front-end (FE)

#### 4-3-1. Functions

Basic functions of the front-end section are (1) to connect with the section of super-high vacuum accelerator, (2) to eliminate of unnecessary off-axis emission, (3) to monitor beam properties for accelerator operation, and (4) to set radiation safety devices.

#### 4-3-2. Arrangement

Fig. 4-3-1 presents the arrangement of the front-end components.

#### 4-3-3. Connection Points

- (1) Upstream: The downstream side flange of the GV below the beam-dump permanent magnet. The GV itself is not included.. (15,000 mm upstream from the uppermost wall of the undulator building)
- (2) Downstream: The downstream side flange of the GV with a beryllium window. The GV is included. (500 mm downstream from the uppermost wall of the experimental hall.)

#### 4-3-4. Specifications of components

##### (1) Common notes

All components are designed with UHV compatibility. Water-cooling system is not employed due to the small power of incident radiation,

##### (2) Main Beam Shutter (MBS)

The MBS, which is composed of an absorber and beam shutter, blocks FEL, spontaneous radiation, and  $\gamma$ -rays. The beam shutter combines tungsten and stainless steel blocks with thicknesses of 400 mm. For the absorber, a graphite block with a thickness of 30 mm and a copper block with a thickness of 200 mm are used. Note that the former part is required for relieving radiation damage of FEL.

(3) Collimator system

The collimator system removes off-axis radiation transported to the optical hutch. The system is composed of two collimators, which are composed of thick blocks of steel with 10-mm beam apertures.

(4) Front-end Vacuum System

The Front-end vacuum system is designed for maintaining an UHV condition, which is directly connected to the undulators and the accelerators without any vacuum window. The system consists of gate valves, a Fast Closing Shutter (FCS) System, and exhaustion pumps.

(5) Front-end Common Support Girder

Two H-shaped beams are placed on the top of two table supports to make a horizontal and vertical datum plane. Pre-aligned vacuum components satisfy the precision of the beam axes by simple installation.

(6) 4-Jaw Slit

The 4-jaw slit is used for eliminating off-axis spontaneous radiation. The blades are made of stainless steel with a thickness of 200 mm. Although this slit is mainly used for cutting off-axis radiation, graphite absorbers are attached on the upstream side of the metal blades in order to avoid accidental radiation damage of metals from the XFEL beam.



## 4-4. Beamline Optics and Transport-Channel

### 4-4-1. Functions

Basic functions of beamline optics and a transport-channel are (1) to tailor radiation properties, (2) to diagnose radiation characteristic, (3) to connect vacuum with the front-end and the experimental station, and (4) to provide safe experimental environment.

### 4-4-2. Arrangement

Fig. 4-4-1 shows the arrangement of the beamline components. A double-crystal monochromator and a couple of double mirror systems is exclusively utilized for covering wide energy range with different bandwidths, as shown in Fig. 4-4-2. The height of the BL3 axis from the floor of the experimental hall is 1400 mm at the entrance of the optics hutch. After the beamline optics of double mirror or double-crystal monochromator, the +20 mm offset is added.

### 4-4-3. Connection Points

- (1) Upstream: The downstream flange of the GV with a beryllium window. The GV itself is not included. (500 mm downstream from the uppermost wall of the experimental hall.)
- (2) Downstream: The GV with a beryllium window in the experimental hutch. The GV is included.

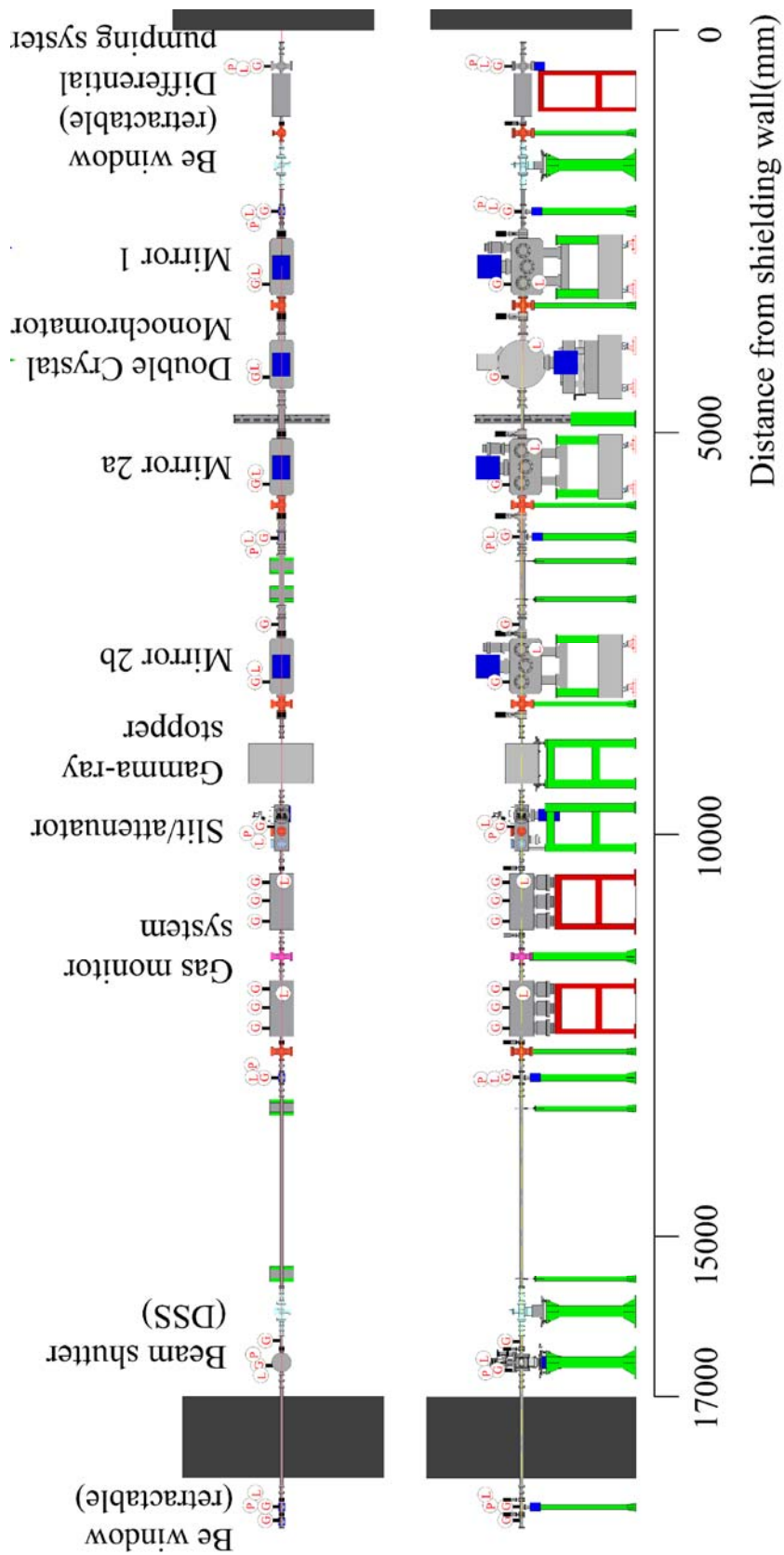


Fig. 4-4-1 Configuration of beamline optics and transport-channel

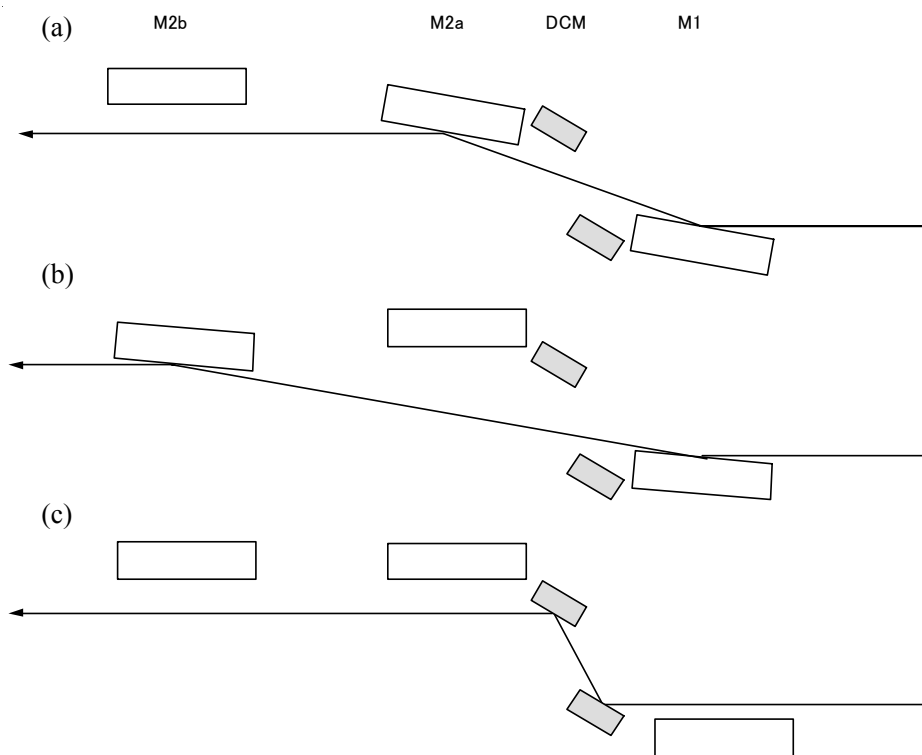


Fig. 4-4-2. Schematic of optics configuration. (a) Double mirror (M1 & M2a) for low-energy use with large glancing angle; (b) double mirror (M1 & M2b) for high-energy use with small glancing angle; (c) double-crystal monochromator.

#### 4-4-4. Specifications of components

##### (1) Mirror

Total-reflection mirrors are used for rejecting higher-energy components including  $\gamma$ -rays. For simple transport of XFEL radiation without additional curvature or disturbance of wavefronts, flat mirrors are employed. The effective reflection area is 350 mm (L)  $\times$  20 mm (W). For avoiding speckles under coherent illumination, the Elastic Emission Machining (EEM) process is applied; the figure error is reduced to below 2 nm (p-v) over the whole area with a roughness of  $< 0.2$  nm (rms). The mirrors are made of silicon with a surface coating of light materials in order to avoid radiation damage. The mirrors are indirectly cooled with water.

Double mirror systems are employed in order to make the output beam parallel to the incident beam. Two different incident angles (2 mrad or 4 mrad) are selectable to change the cut-off energy. The calculated mirror reflectivities for  $B_4C$  and carbon ( $\rho=2.2$  g/cm<sup>3</sup>) are shown in [Fig.4-4-2](#).

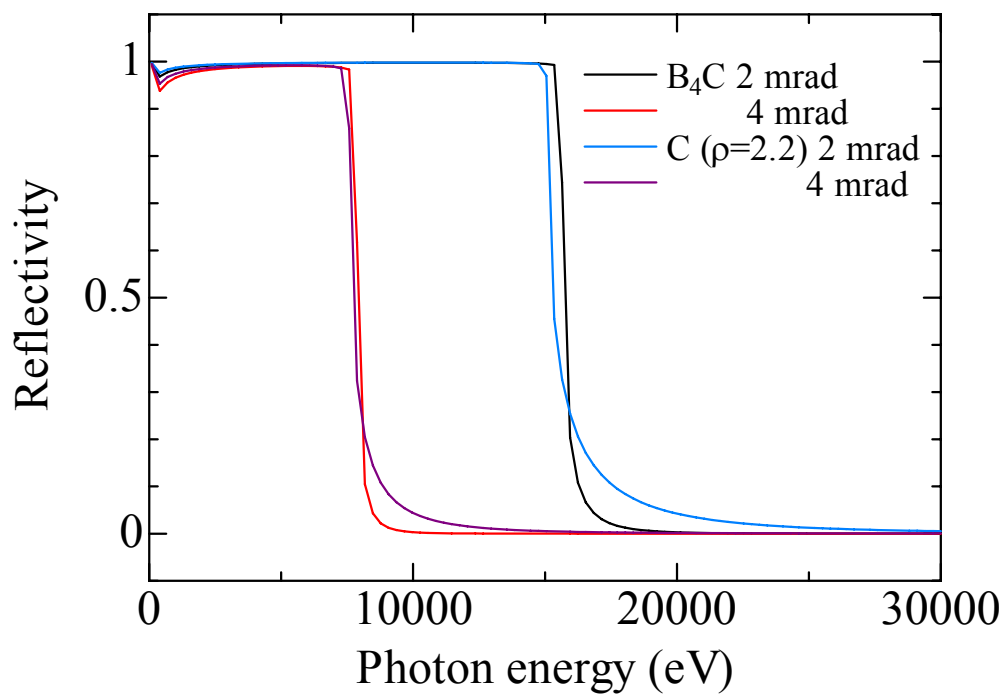
These optical configurations are realized with three mechanical components which control angles and positions of mirrors. A pair of the first (MR1) and the second (MR2a) mirrors is employed for 4 mrad incidence, while another pair of the first (MR1) and the third (MR2b) is used for 2 mrad incidence. The offset value between the incident and the exit beam for the mirror system is designed to be 20 mm in vertical. Thus the distances between mirrors are given by 2.5 m (MR1 to MR 2a) and 5 m (MR1 to MR 2b), respectively.

The axes of the mirror mechanics is schematically shown in Fig. 4-4-3. Ranges and resolutions are summarized in Table 4-4-2. Alignment of the vertical deflection angle ( $R_x$ ) and the vertical position (y) are achieved by the combination of two vertical translation axes. The horizontal translation (x) is used for changing the irradiation area on the surface or switching coating materials. The mirror chamber is designed to be UHV compatibility.

[Table 4-4-1](#) Parameters of beamline optics

	Mirror a	Mirror b	DCM
	For low energy use	For high energy use	
Reflection Surface	light elements		
Diffraction plane	Si 111		
Incident angle	4 mrad	2 mrad	3.7° ~ 30°
Energy range	<7.5 keV	<15 keV	4 ~ 30 keV
Length of optical elements along beam axes	400 mm	400 mm	100 mm
Beam acceptance	1.6 mm	0.8 mm	>6.4 mm

(a)



(b)

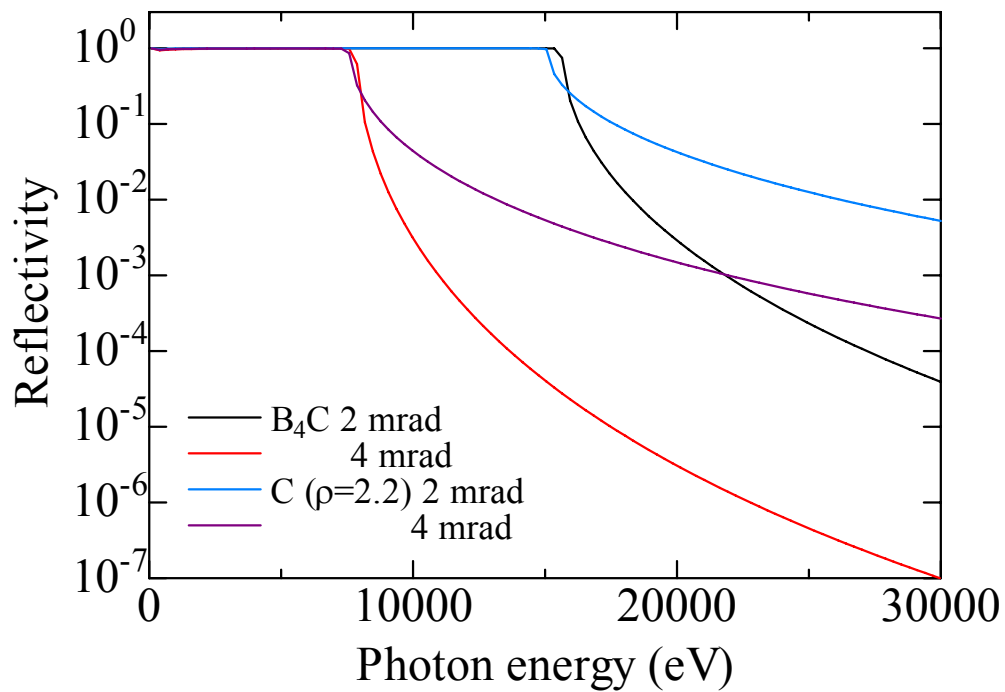


Fig. 4-4-3 Mirror Reflectivity (a) Linear Scale (b) Log Scale

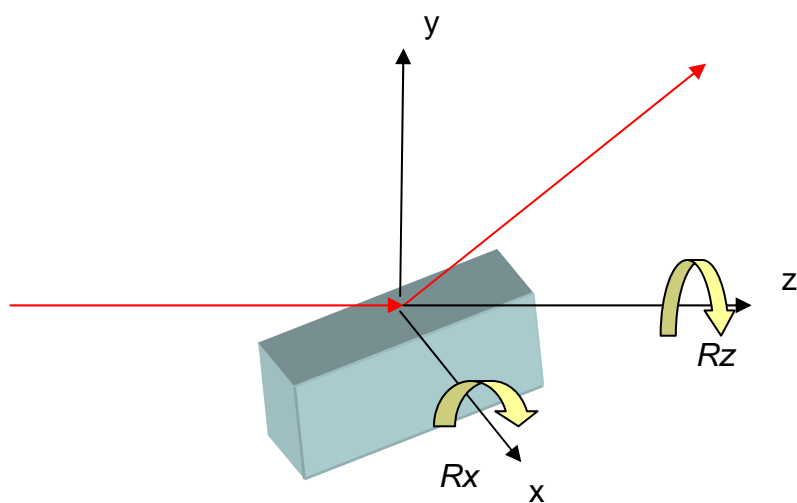


Fig. 4-4-4 Definition of the Mirror Driving Axes

Table 4-4-2 Axes of mirror mechanics

Axis	Purpose	Range	Resolution
Rx	Glancing angle	$\pm 17$ mrad ( $\pm 1.0^\circ$ )	$< 0.6 \mu\text{rad}$
y	Insert/Retract from Optical axis	$\pm 5$ mm	$< 0.5 \mu\text{m}$
x	Switching irradiation area/Coating material	$\pm 5$ mm	$< 5 \mu\text{rad}$
Rz	Tilt adjustment (optionally)	$\pm 5$ mrad ( $\pm 0.3^\circ$ )	$< 100 \mu\text{rad}$

## (2) Double Crystal Monochromator

Double-crystal monochromator (DCM) is used for improving the energy resolution from  $\sim 0.1\%$  of the original FEL radiation to  $< 0.01\%$  at a specific photon energy. Single-crystal silicon is used for the optical element. The monochromator is designed to cover a Bragg angle range from  $3.7^\circ$  to  $30^\circ$ , which corresponds to a photon energy range from 4 to 30 keV with Si 111 diffraction. The number and the strokes of the mechanical stages are reduced in order to improve stability of the monochromatic beam and to maintain clean conditions in the vacuum chamber. This reduction is achieved with the geometry shown in Fig. 4-4-5. The Bragg angle is tuned with a  $\theta$ -rotation table which is linked to a stage located outside the vacuum chamber. The fixed-exit condition for the above Bragg angles range is satisfied with a translation stage for the first-crystal Z1 which changes the gap  $\Delta Z$  between the crystals as,

$$\Delta Z = \frac{h}{2 \cos \theta}, \quad (\text{Eq. 4-4-1})$$

where  $h$  is the offset value. Using the present parameter  $h=20$  mm with  $3.7^\circ \leq \theta \leq 30^\circ$ , the required stroke of Z1 is only 1.55 mm. By permitting a small deviation of  $h$  around the highest Bragg angle (i.e., lowest photon energy), the stroke can be further reduced.

This geometry is supported by allowing a change of the beam position on the crystal surface. By setting the center of  $\theta$ -rotation axis to the symmetric center of the double crystal, the deviations for the first and second crystals are given by

$$\Delta X_1 = \frac{h}{4} \left( \frac{1}{\sin \theta} + \tan \frac{\theta}{2} \right), \quad (\text{Eq. 4-4-2})$$

and

$$\Delta X_2 = \frac{h}{4} \left( \frac{1}{\sin \theta} - \tan \frac{\theta}{2} \right), \quad (\text{Eq. 4-4-3})$$

respectively. Required ranges are evaluated to be  $\sim 70$  mm with the given parameters. A crystal length is set to be 100 mm in order to cover this range.

An angular deviation between the lattice planes of two crystals is controlled with a fine rotation stage of the first crystal  $\Delta\theta_1$ . The tilt deviation is tuned with a rotation stage of the second crystal Ty2.

The crystals are indirectly cooled with water with a temperature control of  $\pm 0.1^\circ\text{C}$ . Radiation damage may be observed in the low energy region. In this case, DCM is used for high-energy x-rays above  $\sim 10$  keV.

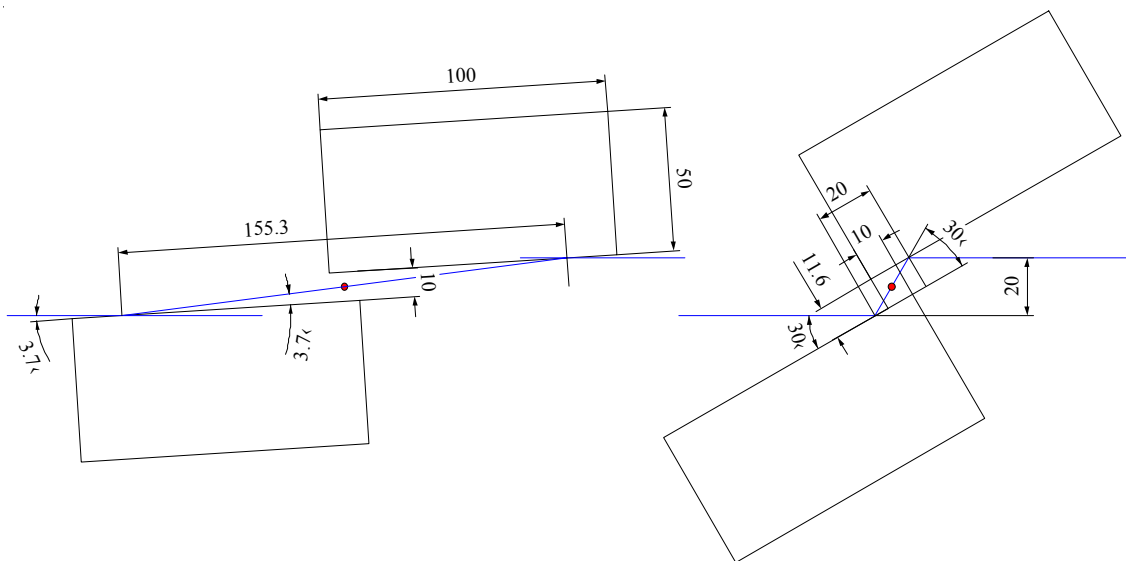


Fig. 4-4-5 Geometry of DCM. Low angle limit (left); high angle limit (right).

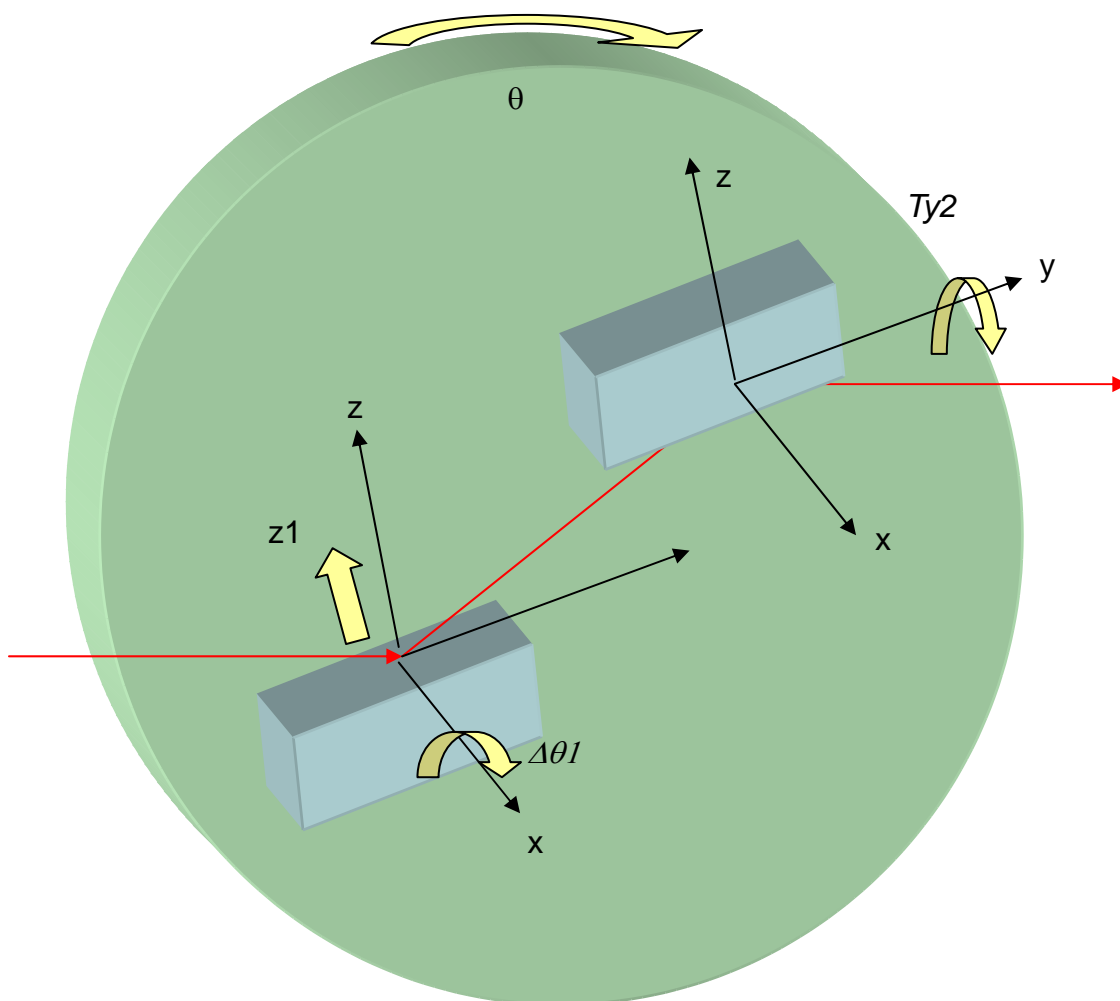


Fig. 4-4-6 Schematic of DCM stages

Table 4-4-3 Specifications of DCM stages

Axis	Purpose	Range	Resolution
Z (manual)	Height adjustment of DCM	$\pm 15$ mm	
X	Horizontal translation of DCM normal to the optical axis	$\pm 20$ mm	100 $\mu$ m
$\theta$	Bragg angle rotation	$-1^\circ \sim 30^\circ$	1 $\mu$ rad w encoder
Z1	Adjustment of gap between crystals	$\pm 0.5$ mm	$< 10$ $\mu$ m
$\Delta\theta 1$	Adjustment of deviation from parallel condition	$\pm 0.5^\circ$	$< 0.1$ $\mu$ rad
Ty2	Adjustment of tilt angle	$\pm 0.5^\circ$	$< 1$ $\mu$ rad

### (3) Attenuator

Attenuators are used for decreasing beam intensity. A speckle-free beam profile is important even under the strong attenuation. For this purpose, two types of devices are prepared; a gas attenuator with a differential pumping system continuously tunes the attenuation ratio by controlling a pressure, while a solid attenuator that consists of silicon wafers with different thicknesses discretely reduces the beam intensity even to  $\sim 10^{-6}$ .

### (4) Radiation shielding devices

A Down Stream Shutter (DSS) is used for blocking FEL and other radiation components while one accesses into the downstream hutches. The shielding block is made of Tungsten. The possible radiation damage of the block is avoided by attaching a graphite absorber in front of the block. Furthermore, a damage sensor consisting of a gas cell is inserted between the two materials.

A gamma-ray stopper composed of a thick lead block is used to stop on-axis g-ray components after the beamline optics. The FEL beam is guided to the downstream components through a rectangular aperture with a size of 17 (H)  $\times$  9 (V) mm. A supplemental shielding plate is placed after the DCM.

### (5) 4-Jaw Slit

A 4-jaw slit is used to eliminate the beam halo and four tantalum blades are independently controlled with stepping motors.

### (6) Vacuum system

The beamline vacuum system is designed to maintain UHV condition with a pressure below  $10^{-6}$

Pa. For the optical components such as the mirrors and DCM, a higher vacuum level below  $5 \times 10^{-8}$  Pa is maintained.

#### (7) Screen monitor

Screen monitors are used for monitoring beam profiles and checking beam positions along the beamline. The beam profile on the fluorescent screen that is tilted to the beam axis is imaged with a commercially-available CCD camera located outside the vacuum chamber. Our target of the position accuracy is 10  $\mu\text{m}$ . Different types of screens and an intensity monitor are switched with a translation stage in order to cover a wide range of intensity. A YAG (Ce) screen is used for detecting the low intensity region, while a B-doped CVD diamond screen with a thickness of 30  $\mu\text{m}$  is prepared for monitoring intense FEL radiation. The latter is expected to have a high damage threshold with a small dose for XFEL radiation. Its linearity has been proven for the high average flux at a SPring-8 beamline (see Fig. 4-4-7) [4-1]. A PIN photo-diode used as an intensity monitor.

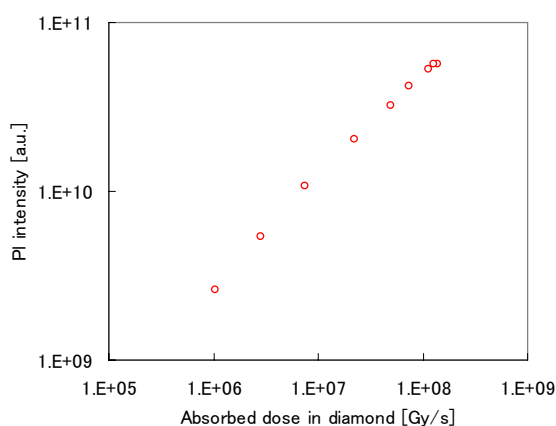


Fig. 4-4-7 Photoluminescence intensity vs. absorbed dose in B-doped diamond foil measured with quasi-monochromatic undulator radiation from BL13XU at SPring-8.

#### (8) Beam position monitor

Beam position monitors regularly provide beam position and intensity information without disturbing experiments performed at the downstream experimental hutch. Our target of the position accuracy is less than 1  $\mu\text{m}$ . The x-ray intensities scattered on a thin foil are monitored with quadrant photodiodes. Shot-to-shot positions of center-of-mass, as well as total intensities, are determined with simple calculations (Fig. 4-4-8). A calibration for beam intensity is made by combining a gas monitor detector (GMD) or a calorimeter.

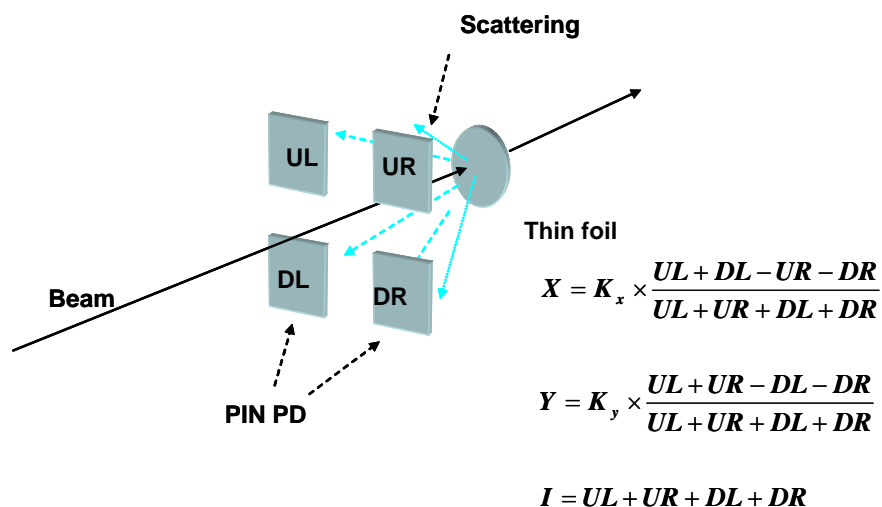


Fig. 4-4-8 Beam Position Monitor using scattering from a thin foil

#### (9) Timing Monitor

The timing monitor is used for synchronizing an external laser to the XFEL for conducting pump-probe measurements. Since both the XFEL and the external lasers have  $\sim 100$  fs jitters to the master oscillator of the accelerator, another kind of accurate timer (post-processing) is inevitably required for fs-resolution pump-probe measurements. Timing measurements of the externally synchronized laser will be made using two independent methods: by comparison with either (a) the timing of the XFEL pulses themselves or (b) the timing of the electron bunches used to produce the XFEL. Which method to use depends on the type of user experiment to be performed.

##### (a) Optical Cross-correlation Measurement

The time difference between the XFEL and the external laser is directly determined using, for example, the transient reflectivity measurement. A post process chamber is installed on the beamline to make the transient reflectivity measurement using an appropriate reflector, such as GaAs.

##### (b) Electro-Optical Sampling (EOS) measurement

The time difference between the external laser pulse and the electron bunches producing the XFEL is determined by an EO effect that occurs in the EO chamber installed in the accelerator. There are three different methods for determining the time difference: spectrum encoding, time encoding and space encoding. Here, space encoding is employed because it has a fairly high time resolution while requiring low laser power. Either ZnTe or GaP is used for the EO crystal. The oscillator output of the external laser is guided into the EO chamber. For several tens of meters between the oscillator and the EO chamber, the laser pulses are transferred through the air or directed through an optical fiber. For the former case, the laser path and the optical components will be covered in order to suppress

the effects of air fluctuation. For the latter, a non-linear effect in the fiber will be suppressed by reducing the peak power using a high chirp, if single-mode fiber is employed. Pulse compression will be applied just before reaching the EO crystal. This design makes the optical system extremely complicated. Photonics fiber may be used to simplify the optical system.

When using a regenerate amplifier with jitters, the time difference between the oscillator and the regenerate amplifier outputs should be measured. This process may be skipped when amplification is made using an OPCPA.

## References

- [4-1] Togo Kudo, Sunao Takahashi, Nobuteru Nariyama, Takeshi Tachibana and Hideo Kitamura, "Synchrotron radiation x-ray beam profile monitor using chemical vapor deposition diamond film", *Rev. Sci. Instrum.* **77**, 123105 (2006).

## 5. Data Acquisition System (DAQ)

### 5-1. Data Acquisition System (DAQ)

#### 5-1-1. Introduction

A SASE XFEL emits X-ray pulses with intensities, ray paths, and timing jitters that vary from pulse to pulse. This makes data analysis for XFEL experiments more complicated than that of conventional SR experiments. XFEL users should take the variation of parameters of each pulse into consideration by referring to the X-ray pulse information when they analyze XFEL data. This can be accomplished by labeling the shot number, *or* “tag”, to the experimental data originating from every XFEL shot. This method of data analysis, although quite common in the high energy physics community, it is not as familiar to the SR and laser communities. Therefore, sufficient information should be provided by the facility when considering which system to utilize.

#### 5-1-2. Basic Plan

The detectors provided by the XFEL facility to the users are connected to a data acquisition system (DAQ) system via data acquisition system (DAQ) boards, which places the tag onto each shot data and send to the storage system, users may also bring their own detector systems. If the user detector can be connected to the DAQ board, the data will be automatically sent to the facility storage. In the case where the user instrument is not compatible with the facility DAQ board, the tag will be provided through a tag generator described below. Technical support for tag handling will be provided by the facility.

#### 5-1-3. Tag

A unique tag number will be allocated to each XFEL pulse. The tag signal provided to users will be 32-bit integer data. The tag-signal together with the pulse date uniquely identifies the pulse used\*. It is recommended that users design their measurement systems which record tag-signals together with their corresponding date and time.

\* 60 Hz operation in 24 hours requires 22.3 bit.

#### 5-1-4. Tag Generator

The tag generator consist of a VME board that counts up the in-coming master trigger, delivers the tag numbers, and outputs two TTL triggers (user triggers) during the user run. The master trigger is provided by TDU (Timing Delay Unit). The schematic diagram is shown in [Fig. 5-1-1](#).

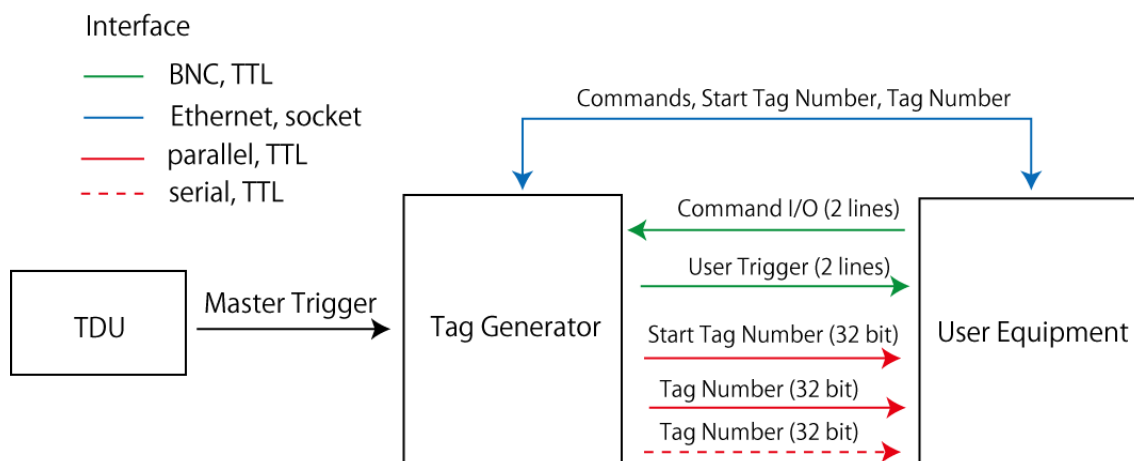


Fig. 5-1-1 the tag generator and its interfaces.

#### (1) Counting up of the master trigger

- In the case when users operate the tag generators, the TDU is set to generate the master trigger 15 msec before the XFEL pulse. The tag generator receives master trigger TTL signal supplied by the TDU and count up the master trigger to calculate the tag. Each tag generator has its own tag in the memory. By resetting the tag of all the tag generators to a specified value while the XFEL is shutdown, all the tag generators have identical tag and synchronized.

#### (2) Delivery of tag number

- User can receive the tag number through Ethernet, parallel IO, or serial IO interface.
- The facility recommendation: how to choose the tag delivery method.
  - A) If the user instrument can record all the shots at the XFEL repetition rate of the user time, Ethernet is recommended. Implementation of this method is simpler than the parallel/serial IO interfaces below.
  - B) If the user instrument cannot record data for all the shots, i.e. the user's system misses some pulse, parallel IO or serial IO is recommended.
- Ethernet interface delivers the initial and the last tag numbers of each user run. Parallel and serial IO interfaces provide the initial and the last tag numbers as well as the real-time tag numbers.

#### (3) Output of user trigger

- The tag generator has two user triggers at TTL level. These are only generated during the user run. Each trigger has a specific delay time to the master trigger. Each delay time can be adjusted by user via GUI interface, or Ethernet socket communications.

#### (4) Start and Stop commands

- Users can send the start/stop commands through Ethernet socket communication, or a TTL signal via BNC connectors.

#### (5) Operation

- Fig. 5-1-2 shows the operation sequence. A start command should be sent to the tag generator to initiate a user run. During the user run, user triggers are delivered to the user equipment. The XFEL pulse can be stopped off during the user run by x-ray shutter. Users can send the start command by pressing the start button on a GUI interface of a beamline PC, or by sending start command through Ethernet socket, or set high of TTL level on the start command line. When a stop command is sent to the tag generator, the user trigger immediately stops and the user run is terminated. The initial and the last tag numbers are stored in the tag generator's memory. These numbers can be obtained by watching the GUI interface, or via Ethernet socket communications, or parallel I/O.
- Users who need highly accurate time delays to nsec accuracy can use timing signals in the, NIM and Pecl supplied by the TDU (Timing Delay Unit) installed at the beamlines by the facility. Tags will be given by using the user trigger from the tag generator as veto signals.
- The user triggers is delayed to the master trigger. Each delay times of the user trigger can be configured through a GUI on the beamline's PC, or through socket communications.
- Tag signals will be "0" by reaching at 32-bit. This means that the unique allocation of pulses is impossible by using only the tag signal. Therefore, users are strongly encouraged to record the dates and times of their data acquisition. An application of the tag generator is shown in Fig. 5-1-3. Users are strongly encouraged to record the dates and times of their data acquisition with an accuracy of at least 1 min. The facility will provide time data using an NTP server, so users are requested to synchronize their system clock with the signal.

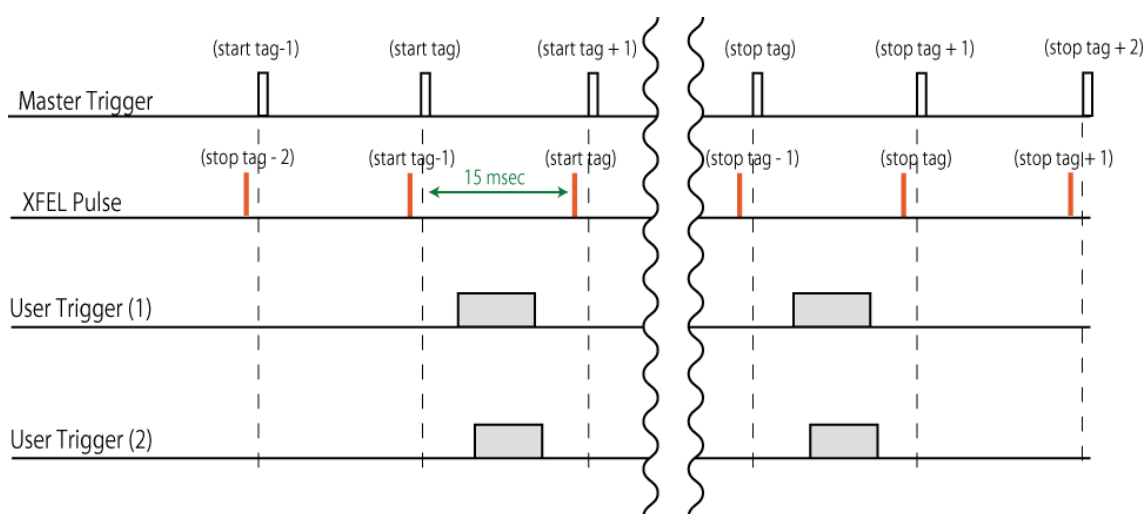


Fig. 5-1-2 Timing chart of the tag generator for a user run.



detector having 2 bytes of data/pixel should have a data transfer rate of 1 Gbps, whereas a 9 Mpixel detector should have 10 Gbps. The DAQ system has two different outputs: a log output to record all data, and a monitor output to allow users to make real time evaluation of the experimental results (Fig. 5-1-5).

#### (1) Data Transfer for Monitor Output

- Skipping data transfer if necessary.
- The skipping rate can be defined by users.
- The data for the monitor should be the same when referred to multiply. This is assured, e.g., by producing tag signals with the first digit “0” at 6 Hz when a skipping rate of 10 is designated at 60 Hz operation.
- The output from each monitor will be available to many PCs.
- Monitor outputs will be asynchronous to maintain real-time operations.

#### (2) GUI for Monitor Output

- Time-series data for 0-D and 1-D detectors, and image data for 2-D detectors will be displayed.
- Monitor data can be saved to files.
- Data analysis can be processed with the data analysis libraries.
- The data analysis libraries contain both standard and user-optional libraries. The standard library provides the tools to give a standard deviation, peak position, median position and total signals of a time-series data, as well as display the results.
- The detailed spec for the libraries is TBD.

#### (3) Log Output

- All data will be saved with the corresponding tag signal.
- Metadata such as the experiment date, the user’s run number, the experiment proposer’s name and comments can also be saved.
- The detailed spec for the Log Output is TBD.

#### (4) GUI for Log Output

- Can download the Log, and display the Metadata as well as the simplified data.
- Can perform data analysis for all or a part of the data using the data analysis libraries.

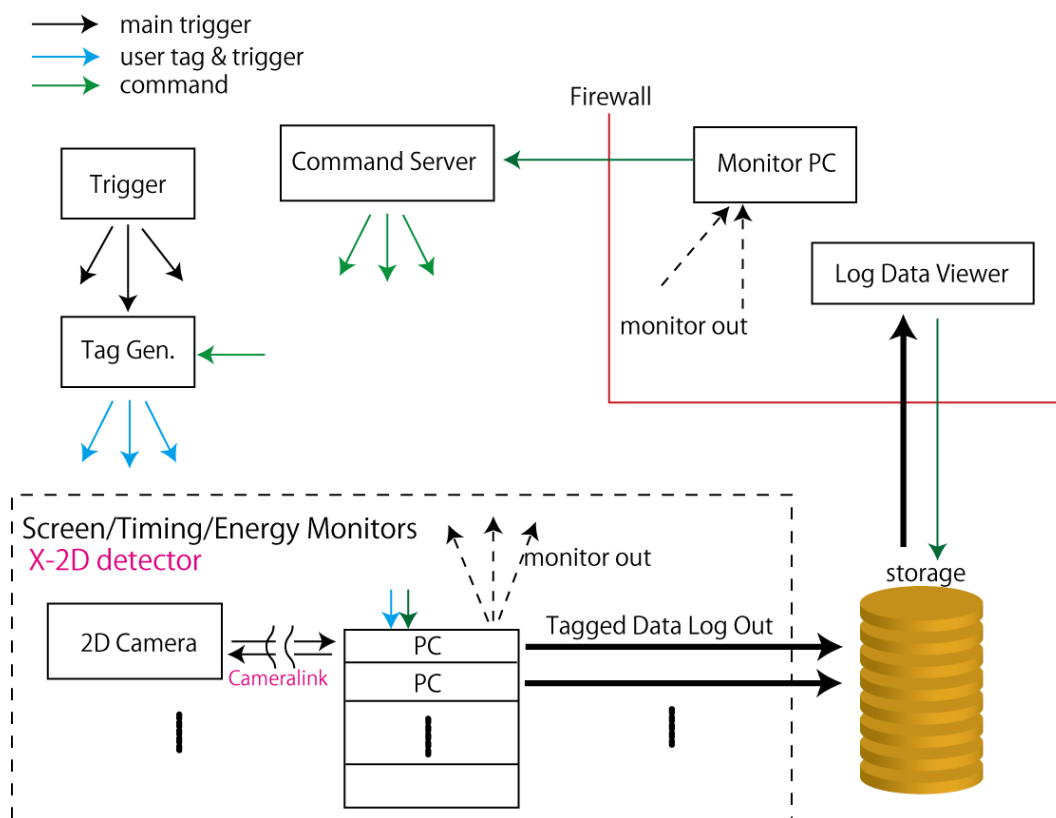


Fig. 5-1-5 DAQ System Configuration

### 5-1-6. Detectors and DAQ boards

The DAQ system takes care of the following detectors and IF boards:

#### (1) 0-D detector

- A medium speed 24 bit ADC, a high speed 12 bit ADC, and a DIO board are equipped for the 0-D detectors.
- PIN photodiodes will be used for the beam position monitors. The four PINs should all have similar sensitivity to X-rays.

#### (2) 1-D detectors

- 1-D detectors can be replaced with 2-D detectors, so their introduction for user applications merits careful consideration. Any of the following may be used for equipment monitors:
  - 1-D detector for fast energy monitors,
  - 1-D detector for slow but high-precision energy monitors,
  - 1-D detector for EO monitors.

#### (3) 2-D detectors

- Visible CCD cameras
- TV cameras for viewing screen monitors

- X-ray 2-D detector (see the next section)
- The user's camera can be connected to the DAQ system if necessary (with permission from the facility). The recommended interface for the 2-D detector is the Cameralink up to the base configuration.

#### 5-1-7. Visible CCD Camera

The visible CCD camera should be more than 60 fps (frame per second) and externally triggerable. The interface should be the Cameralink. The camera selected should be applicable for a wide variety of potential applications including the user's experiments. The spec should be the same as that for the beamline monitors.

#### 5-1-8. Data Storage

- Data should be saved in the data storage device.
- The data transfer and storage for the detectors composed of multiple element modules will be made by using multiple PC servers. This configuration allows the transfer speed and the saving speed to be maintained by adjusting the number of servers and data storage devices. This simplifies any future expansion required.
- Users should transfer their data to personal devices after completing their experiments.
- The data on the facility storage devices will be discarded after approximately 3 months.
- The unique run-number should be recorded for each measurement run.
- The data is accessible by users via the internet.

## 5-2. X-Ray 2-D Detectors

### 5-2-1. Introduction

Users can use X-ray 2-D detectors developed by the facility. XFEL has quite different characteristics from other existing sources, accordingly, the 2-D detectors for XFELs should have unique performance optimized for XFEL applications.

### 5-2-2. Outline of the required specifications

The following two features of XFEL applications are important from the viewpoint of the detector development:

- (requirement 1) Data acquisition should be made pulse by pulse.
- (requirement 2) The total power in one pulse is extremely higher than that of SR. This makes the photon number incident on one pixel of the detector capable of increasing from approximately a few to  $10^6$ .

Requirement 1 indicates that the DAQ system should have an image capture rate of 60 fps (frames per second) synchronizing to a 60 Hz operation of the XFEL. In addition, the sensor should not

produce long-life afterimages in order to avoid the mixing of multiple frame data.

To fulfill requirement 2, some processes degrading the linearity of the sensor response can occur when extremely intense X-rays impinge on the detector. This process has not been investigated, to our knowledge, additional R&D will be necessary.

Conventionally, 2-D X-ray detectors combining the fluorescence screen with a CCD detector have been widely used in many SR facilities. X-ray photons are converted to visible fluorescence photons in the screen and then imaged with CCD detector having higher sensitivity in the visible range. However, they are problematic for use at XFEL beamlines because they are easily damaged with radiation, and have strong afterimages. On the other hand, direct X-ray detection with Si semiconductor detectors utilizes the electron-hole pair creation in the photodiode when X-rays are absorbed. Electrons and holes drift to opposite directions in the photodiode, and eventually converted to voltage signal inside the detecting device. The voltage signal will be converted to a digital signal using an analogue-to-digital converter (ADC).

One way to fulfill requirement 1 is to accelerate the detection process. However, aggressive-force acceleration will result in noise increase. A better solution may be to adopt parallel readings to make the total throughput faster.

Even experts in detector technology have never found a solution to satisfy requirement 2. There is a report suggesting that the maximum detectable 10 keV X-ray intensity for Si detector is approximately 2,500 photons in a  $50 \times 50 \mu\text{m}^2$  pixel. If 106 X-ray photons are uniformly absorbed in a pixel with the volume of  $100 \times 50 \times 50 \mu\text{m}^3$ , the carrier density reaches  $1016 \text{ e/cm}^3$ , which corresponds to the doping density of typical photodiodes. Therefore, the device would not work normally because the electric field of the depletion layer would be screened by carriers produced by X-ray absorption. Preliminary tests (unpublished) showed the effect became noticeable when 2,500 X-ray photons of 10 keV were absorbed in a  $50 \times 50 \mu\text{m}^2$  pixel, resulting in deterioration of the spatial resolution (point spread function) of the 2-D detectors due to changes in the detector response.

### 5-2-3. Development Strategy

There are many different requirements for the detectors. No existing detector can fulfill all the requirements, nor can commercially available sensor devices. Therefore, new sensor, driving and read-out circuits should be developed. In selecting the detector system, an imaging speed of 60 fps should be indispensable, and a Full Well Capacity should be highly prioritized. Large size detectors will be built using modular construction. However, leaving blind areas between modules is believed to be crucially important for such applications as coherent X-ray diffractive imaging. The size of the allowable blind areas will be specified when the estimation is made.

Currently, two detector systems are under development. One of these is a multi-port charge-coupled device detector (MPCCD) which is described below. This development project is

classified as Stable Detector program where the project top priority is the timeline; the detector should work at the time of XFEL lasing. The other detector is based on silicon-on-insulator technology managed as Advanced Detector program aiming at higher performance with lower cost.

#### 5-2-4. Stable System: MPCCD Detector System

##### (1) Introduction

The multiport CCD detector system is composed of (a) sensor modules, (b) control circuits, (c) data transfer frontends, and (d) data storage devices. Data buffered in the data transfer frontends will be transferred to the data storage devices through the gigabit Ethernet.

##### (2) Sensor Modules

The development of detecting devices requires both a considerable investment and a long period of time. Therefore, it is desirable to use one detecting device for as many experiments as possible. For example, some experiments need a center hole in the detector, but others do not. The present proposal for modular sensor devices enables the user to switch from one type to the other by rearranging the sensor modules (Fig.5-2-2). The pixel number of the unit module has  $1024 \times 512$  pixels with  $50 \mu\text{m}$  square shape. Fig. 5-2-3 illustrates the schematic structure of the module. Target performance is listed in Table 7-2-1.

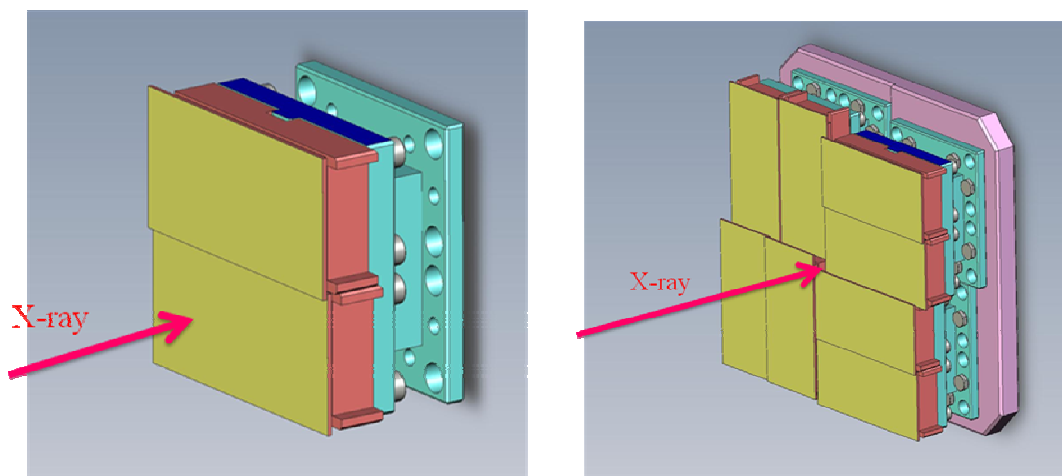


Fig. 5-2-2 Structures of sensor module arrays for  $1\text{k} \times 1\text{k}$  pixel detector (left), and  $2\text{k} \times 2\text{k}$  pixel detectors with a center hole (right).

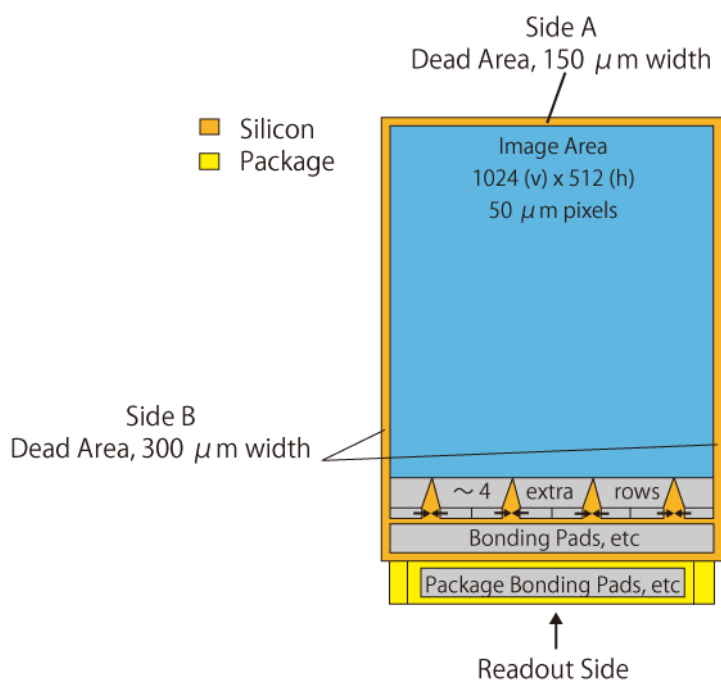


Fig.5-2-3 Schematic Structure of the MPCCD sensor module with 8 output readout nodes indicated as arrows.

Table 5-2-1 Target Performance of multi-port charge coupled device (MP-CCD) detector

Parameter	Target Value	Units	Comments
Pixel size	50 x 50 100 x 100	$\mu\text{m}^2$	in 2 x 2 binning mode
Operating Temperature	0 ~ -50°C	°C	
Detection Efficiency	80 20	%	6 keV x-rays 12 keV x-rays
System Noise	< 0.2 < 330	photons e-	for 6 keV x-rays
Full Well Capacity	5 3100 20 12400	Me-/pixel photons/pixel Me-/pixel photons/pixel	for 6 keV x-rays in unbinned mode for 6 keV x-rays in 2x2 binning mode
Frame Rate	> 60	Hz	
Dead area width	< 300	$\mu\text{m}$	3 effective pixels in 2x2 binning mode
Tiling Capability	3-side buttable	N/A	
Radiation Hardness	$4 \times 10^{11}$	photons/pixel	for 12 keV x-ray

## 6. Civil Engineering: Experimental Facility

### 6-1. Outline

This chapter describes a basic plan of the Experimental Facility including the Experimental Hall, the Preparation Rooms, and the Machine Rooms. This plan was settled by the Joint-Project Team at the end of January, 2008. Following detailed design works, the construction will begin in March, 2009, and complete in May, 2010.

The following points have been taken into consideration:

- (1) The structure of the floor of the Experimental Hall should be designed to avoid subsidence in the future. Particular attention must be given to reduction of vibration. Note that the geologic ground condition consists of medium-hard rock with high stability.
- (2) The building of the Experimental Hall should be designed to have high stability against external vibration and temperature fluctuation.
- (3) The Preparation Rooms should accommodate basic infrastructure. Attention should be paid for realizing flexible and multipurpose utilization.

A location map, a floor plan, and a sectional elevation view of the Facility are attached in [Fig. 6-1-1](#), [Fig. 6-1-2](#) and [Fig. 6-1-3](#), respectively. Although the area of the Facility is restricted by the peripheral road, beamlines can be extended towards the storage ring building through the culverts under the road.

### 6-2. Experimental Hall

XFEL experiments are conducted in the Experimental Hall, which contains radiation shielding hutches, beamline components, experimental instruments, and remote control systems.

#### (1) Size

The Experimental Hall is 56-m long (in the direction of the beam axis) and 31-m wide. Intervals between XFEL beamlines are 3 m. The distance from the undulator (No. 18) for BL3 to the partition wall to the Hall is about 73 m.

#### (2) Floor

The floor of the Experimental Hall is cast with 1.3-m thick concrete. The floor supports a load of 2 t/m<sup>2</sup>. A flatness of the floor is controlled within  $\pm 10$  mm. The floor surface is coated with an epoxy resin paint to avoid dusts from the floor concrete. The height of the XFEL beam from the floor level is set to be 1.4 m. In order to avoid vibration, the floor should be separated from the foundation of the Machine Rooms that contains air-conditioning and water-circulating machines. Polishing of the floor is considered for utilizing optical benches with air-pad carriers.

#### (3) Overhead Crane

An overhead crane (max lifting weight of 2.8 t; lifting height of 7 m) is prepared in the Hall.

#### (4) Carry-in Entrance

The carry-in entrance with a size of 4 m × 4 m is settled on the south side of the Experimental

Hall. The entrance door on the north side of the hall is 2-m high and 2-m wide.

#### (5) Air Conditioning

Temperature in the Experimental Hall is stabilized within  $\pm 2$  °C. The roof and walls are thermally insulated from outside. Vibration caused from the air-conditioning system should be avoided.

#### (6) Utility

Electrical switch boards, canisters for coolant water and compressed air, and ports for air-conditioning are prepared for each beamline. Scrubber can be installed for local exhaustion in the future.

### **6-3. Experimental Preparation Room**

The Experimental Preparation Rooms are used for preparation of experimental instruments. 5 rooms are settled inside the radiation control area next to the Experimental Hall. The size of the room is 7 m × 10 m × 3 m (height) with an entrance size of 2 m × 2 m. The floor load is 1 t/m<sup>2</sup>.

Each room has electrical switch boards, although clean water and an experimental drainage system are not available.

### **6-4. Sample Preparation Room**

The Specimen Preparation Rooms are used for preparation of samples. Outside the radiation control area, 5 rooms are settled on the second floor of the Facility. The size of the room is 7 m × 10 m × 3 m (height) with an entrance size of 2 m × 2 m. The floor load is 0.5 t/m<sup>2</sup>.

Each room has electrical switch boards. Some of rooms provide clean water and experimental drainage systems.

### **6-5. Carry-in Room**

The carry-in room is settled as a buffer room for transporting experimental instruments from/to the Experimental Hall. This room is located outside the radiation control area. The size of the carrying room is 14 m × 7 m × 5 m (height) with a floor load of 2 t/m<sup>2</sup>. The size of the entrance is 4 m × 4 m. The overhead crane is not available.

### **6-6. Noise Shielding**

Special attention should be paid for designing signal grounds at the Experimental Hall in order to suppress EMC and AC-line noises.

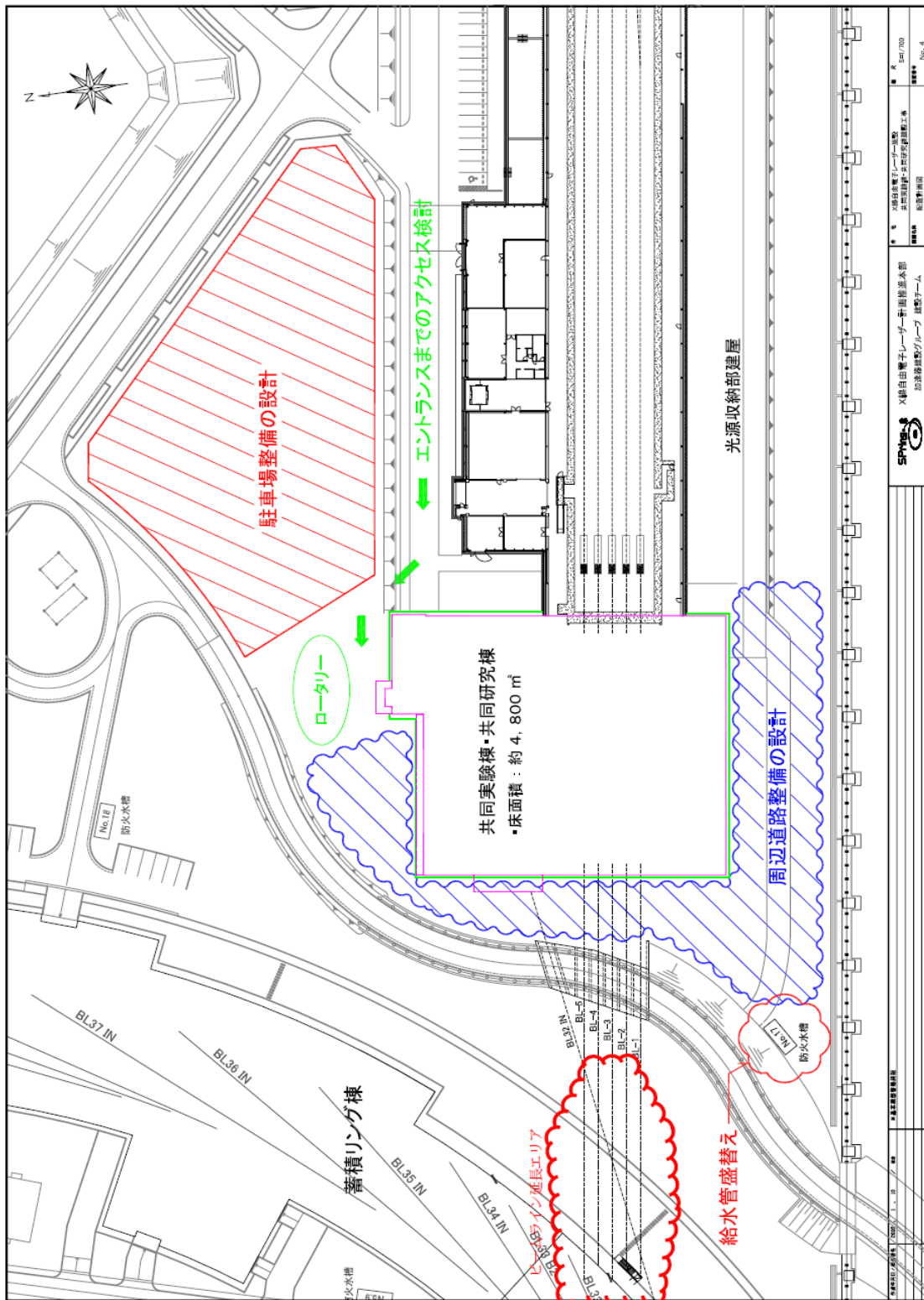


Fig. 6-1-1 XFEL Experimental Facility - floor plan.





## APPENDIX

### A1. Dose Estimation for XFEL

#### A1-1. Introduction

The irradiation tolerance of optical elements for XFEL is a critical issue because the pulse-energy of XFEL within short periods is extremely high. The optical elements to be used in the first beamline will be classified according to their purpose as follows:

Table A1-1-1 Optical Elements

Classification	Candidate Materials	Distance from the source, $L$ (m)
(A) Beam stopper (Shutters, collimators)	Combination of light and heavy materials	75 ~ 150
(B) Vacuum windows	Be or diamond crystals	75 ~ 150
(C) Monochromator crystals	Si or diamond crystals	100 ~ 150
(D) Total reflection mirrors	Light elements	100 ~ 150

Tolerance estimations were made by comparing the absorbed XFEL energy in a material expressed as absorption energy per constituting atoms (unit: eV/atom) with the materials' threshold energy for melting. Evaluations were made using conventional absorption coefficients for (A), (B), and (C), and an incident-angle-dependent absorption coefficient with extinction correction for (D).

#### A1-2. Light Source Parameters (subject to change according to the progress of machine development)

Photon numbers per SASE pulse,  $N_p$ , beam size,  $\sigma$ , and beam divergence,  $\sigma'$  were calculated using SIMPLEX code. The photon number came from the SIMPLEX panel display, while the beam size and divergence were calculated using a simulation. Dependence on the photon energy,  $E_p$ , was calculated by changing the electron beam energy,  $E_B$ , from 2 to 8 GeV for  $E_p < 10$  keV with a fixed K-value of the undulator (#1-#7). For  $E_p > 10$  keV, it was calculated by changing the K-value with fixed electron beam energy of  $E_B = 8$  GeV (#7-#9). The following beam parameters were also used for the calculation:

Normalized emittance	: 1 $\pi$ mm.mrad
Energy Spread	: 1E-4
Peak Current	: 3 kA

Charges/Pulse	: 0.2 nC (67 fs full-width rectangular pulse)
Undulator Periods	: 1.8 cm
Undulator Length	: 5 m (1 segment)
Average $\beta_x, \beta_y$	: 26 m

The resulting values for  $N_p$ ,  $\sigma$ , and  $\sigma'$  are shown in the following table. The last column lists the ratio between the emittance and the wavelength:

$$R = \sigma \sigma' / (\lambda / 4\pi) \quad (\text{Eq. A1-2-1})$$

Although Gaussian diffraction-limited light will result in  $R = 1$ , the present calculation produced  $R = 1.5$  as an average value. The photon energy dependences of  $N_p$ ,  $\sigma$ ,  $\sigma'$ , and  $R$  are shown in Fig. A1-2-1 to A1-2-3.

Table A1-2-1 Calculated  $N_p, \sigma, \sigma'$

#	$E_B$ (GeV)	$K$	ID segment number	$E_p$ (eV)	$\lambda$ (nm)	$N_p$ (photons/pls)	RMS $\sigma$ ( $\mu\text{m}$ )	RMS $\sigma \sigma'$ ( $\mu\text{rad}$ )	$R =$ $\sigma \sigma' / (\lambda / 4\pi)$
1	2	2.18	5	625	1.98	4.90E+12	44.5	5.54	1.56
2	3	2.18	6	1410	0.882	2.40E+12	30.8	1.89	0.83
3	4	2.18	8	2500	0.495	1.40E+12	43.7	1.44	1.60
4	5	2.18	10	3910	0.317	8.80E+11	42.7	0.957	1.62
5	6	2.18	12	5630	0.22	5.70E+11	36.8	0.721	1.51
6	7	2.18	15	7660	0.162	3.80E+11	37.1	0.512	1.48
7	8	2.18	18	10000	0.124	2.60E+11	35.9	0.412	1.51
8	8	2	18	11255	0.110	1.91E11	27.5	0.443	1.40
9	8	1.754	18	13300	0.093	1.15E+11	21.1	0.399	1.13

The following calculation uses the above listed  $N_p$  (and its interpolation), and averaged  $\sigma$  values of #1 through #7, 38.8  $\mu\text{m}$  (#8 and #9 do not reach saturation). Divergence  $\sigma'$  was determined by Eq. A1-2-1 so that  $R = 1.5$  and  $\sigma = \sigma_{\text{ave}}$

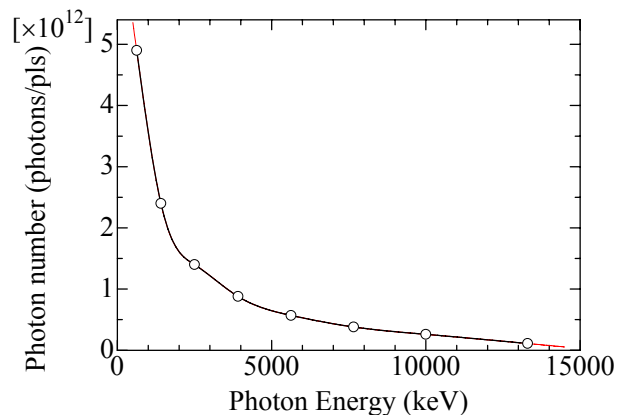


Fig. A1-2-1: Photon number per pulse vs. Photon Energy

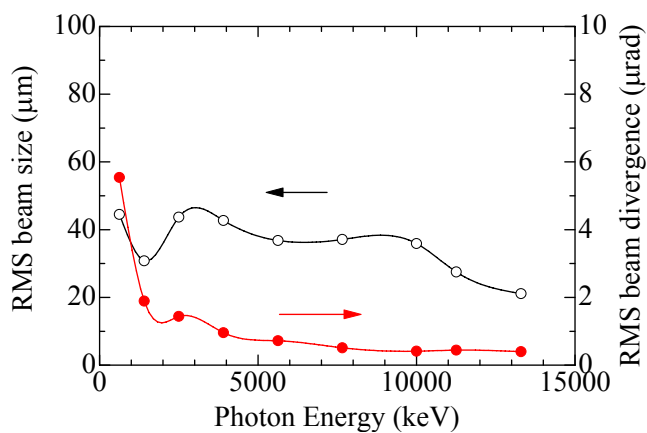


Fig. A1-2-2 Energy dependence of the beam size and divergence.  
The solid lines show spline interpolations.

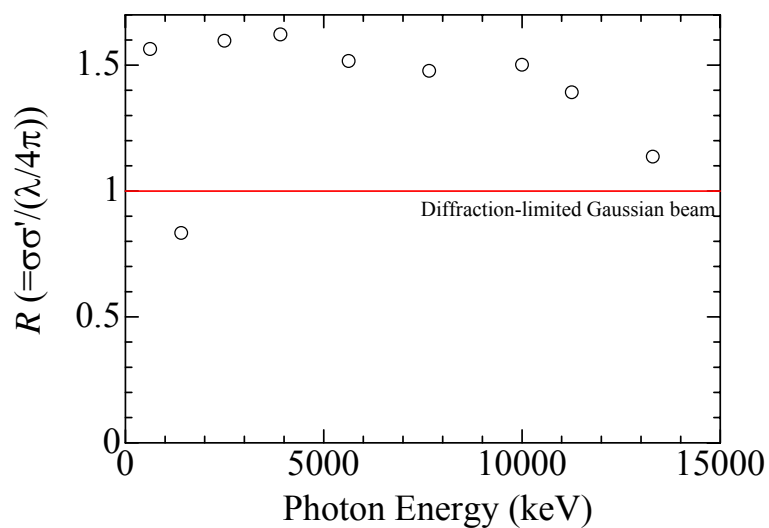


Fig. A1-2-3 Energy dependence of the parameter R

### A1-3. Conventional Absorption Dose

Absorption Dose,  $D$ , under conventional absorption condition is estimated by the formula:

$$D = \frac{\mu N_p e E_p A}{2\pi\sigma_L^2 \rho N_A} \quad (\text{Eq. A1-3-1}),$$

where the following symbols are used for designating the parameters:

$\mu$ : absorption coefficient

$\sigma_L$ : rms beam size at the sample position, distance  $L$  from the source.

$A$ : average atomic weight

$\rho$ : average density

$N_A$ : Avogadro's Number.

Energy dependence (from 0.5 to 15 keV) of the doses for Be, B<sub>4</sub>C, Graphite, Diamond, SiC, Si and Cu, calculated at a point 100 m downstream from the source are shown in Fig. A1-3-1. The source-to-sample distance dependence of the doses calculated at a photon energy of 1 keV and 5 keV is shown in Figs. A1-3-2 and A1-3-3. The calculated results can be summarized as follows:

- (1) The melting threshold of Cu can be surpassed at lower energies or near the absorption edge for an even longer source-to-object distance ( $L \sim 100$  m) (Fig. A1-3-1). Therefore, it is recommended not to use Cu for the first beam-blocking component.
- (2) Lighter materials such as Be, B<sub>4</sub>C, Graphite and Diamond can be used immediately downstream of the light source for higher energy photons ( $E_p = 5$  keV) (Fig. A1-3-2). For lower energy photons ( $E_p = 1$  keV), the melting threshold is surpassed immediately downstream from the source, but the threshold is more than one order of magnitude larger than when the distance is greater than 75 m (Fig. A1-3-3). These materials are suitable candidates for beam blocking and window materials.
- (3) The dose for the crystal monochromators using Si and Diamond crystals placed at  $L = 100$  m can be estimated from Fig. A1-3-1. The margin to the threshold of Si at high energies ( $E_p > 6$  keV) is more than one-order of magnitude, but it is less than one-order of magnitude at lower energy ( $1.98 \leq E_p < 6$  keV, minimum energy is determined by the allowable Si 111 reflection). The maximum dose around  $E_p \sim 2$  keV is not more than the threshold value. Diamonds have a much greater margin to the threshold value over the entire energy range ( $E_p \geq 3.02$  keV) covered with 111 reflection.

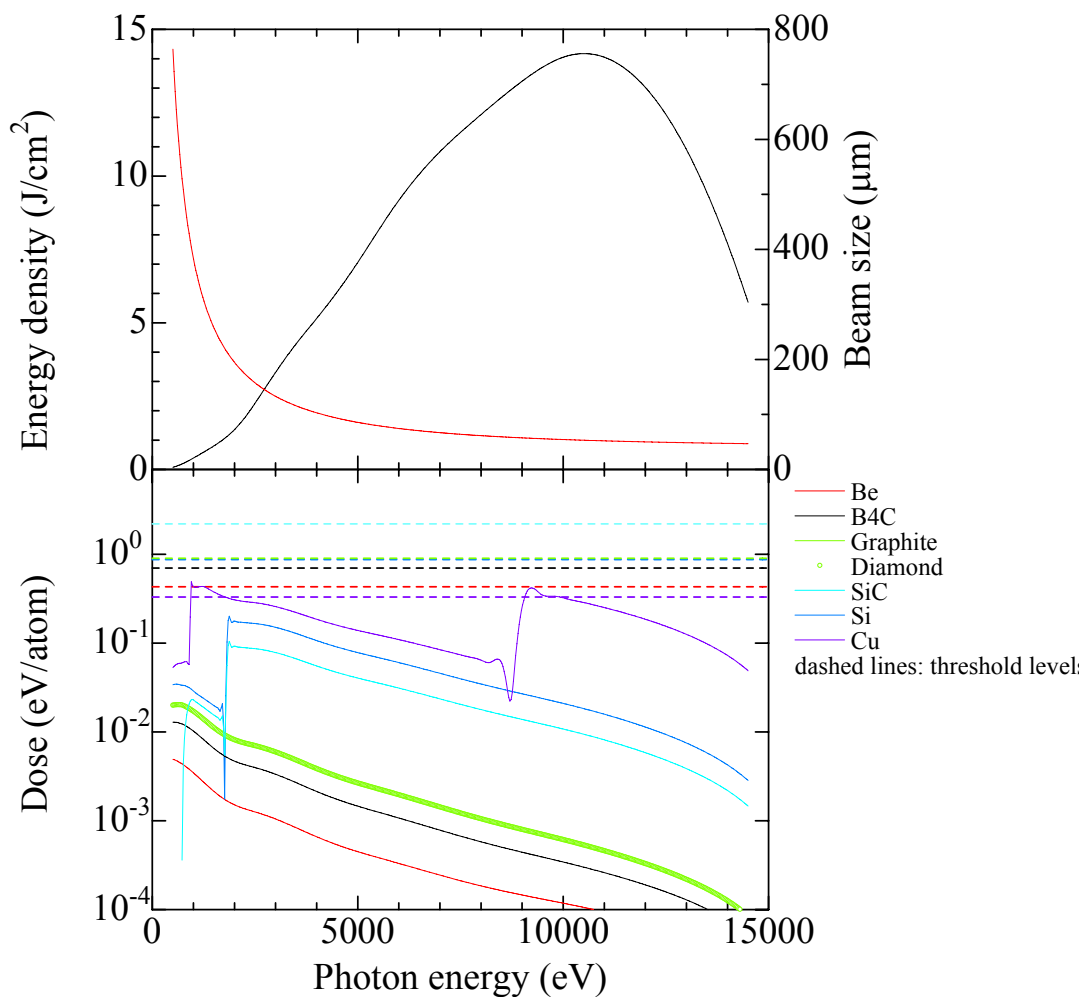


Fig. A1-3-1 (above) Photon energy dependence of energy density and beam size of SASE FEL, (below) Photon energy dependence of doses. Both calculations are made for  $L=100$  m.

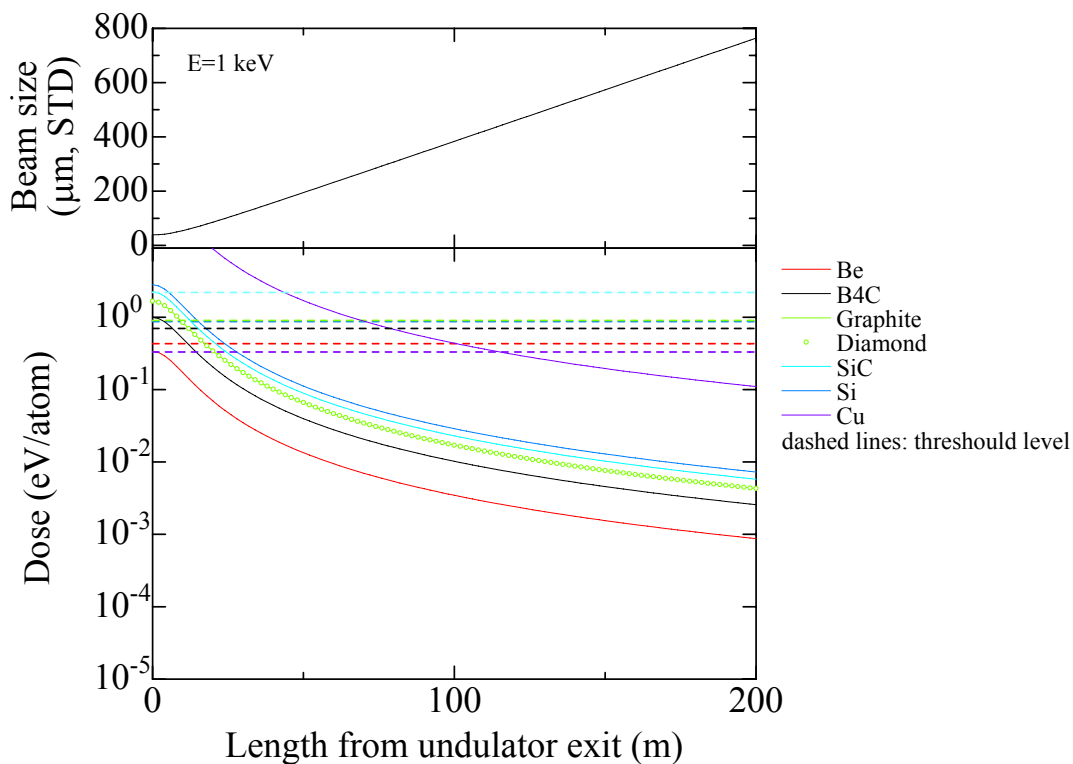


Fig. A1-3-2 Distance dependence of the Dose and Beam Size at  $E_p = 1$  keV

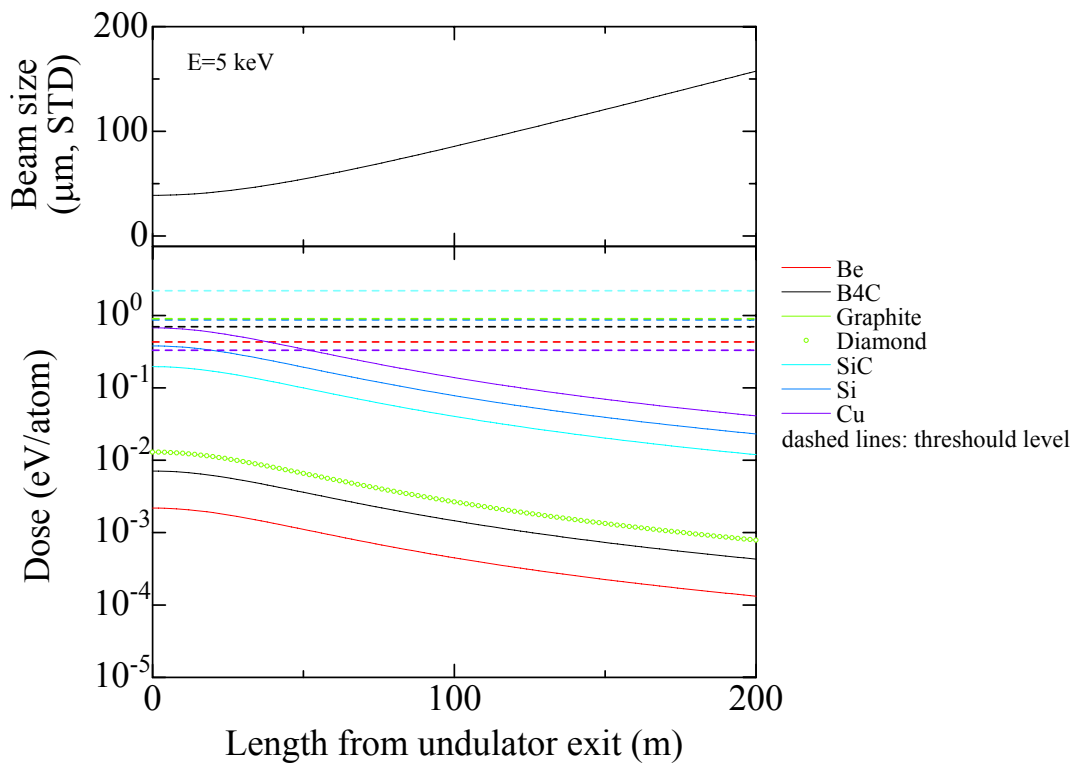


Fig. A1-3-3 Distance dependence of the Dose and Beam Size at  $E_p = 5$  keV

#### A1-4. Dose under Total Reflection Conditions

The dose under the total reflection condition is given by Eq. A1-4-1,

$$D = \frac{\mu_R(\theta) N_p e E_p A (1-R) \sin \theta}{2\pi \sigma_L^2 \rho N_A}, \quad (\text{Eq. A1-4-1})$$

where  $R$  represents reflectivity, and the incident-angle-dependent absorption coefficient  $\mu_R(\theta)$  is expressed as a function of the complex refraction coefficient,  $n=1-\delta+i\beta$ , as

$$\mu_R(\theta) = \frac{2\sqrt{2}\pi}{\lambda} \sqrt{\sqrt{(2\delta - \theta^2)^2 + 4\beta^2} + 2\delta - \theta^2}. \quad (\text{Eq. A1-4-2})$$

When the glancing angle,  $\theta$ , is far above the critical angle,  $\sqrt{2\delta}$ , Eq. A1-4-1 approximates Eq. A1-3-1.

The calculated results for the glancing-angle dependence of the dose and reflectivity for  $E_p = 10, 5,$  and  $1$  keV for  $L=100$  m are shown in Figs. A1-4-1, A1-4-2, and A1-4-3. The calculated results for energy dependence of the dose and reflectivity with a fixed glancing angle are shown in Figs. A1-4-4 and A1-4-5. The calculated results for the doses for a fixed length ( $L_M = 50$  cm) mirror, where the glancing angle is varied so that the mirror acceptance  $\theta L_M$  is six times the beam size  $\sigma_L$  are shown in Fig. A1-4-6.

Mirror materials of Au, Si, SiC and graphite ( $\rho=2.2$  g/cm<sup>3</sup>) were assumed. Surface roughness is not taken into consideration. The results are summarized as follows:

- (1) The dose of the Au mirror surpassed the threshold near the critical angle (Figs. A1-4-1, A1-4-2).
- (2) The dose of the Si mirror came nearer to the threshold near the critical angle but did not surpass it (Figs. A1-4-1 and A1-4-2). When fixed at the glancing angle of  $\theta = 0.1^\circ$ , the dose was two orders of magnitude smaller than the threshold (Fig. A1-4-4), and the glancing angle of  $\theta = 0.2^\circ$  gave the dose a margin of one order of magnitude (Fig. A1-4-5).
- (3) The absorption dose of SiC was similar to that of Si. The higher threshold made a larger margin.
- (4) The dose of the graphite was two orders of magnitude less than the threshold even around the critical angle, because of a smaller absorption rate per atom (Figs. A1-4-1, A1-4-2).
- (5) Fig. A1-4-6 shows that the glancing angle  $q$  was much smaller than the critical angle when the condition of  $\theta L_M = 6\sigma_L$  was maintained for a mirror with  $L_M = 50$  cm. Accordingly, the dose would have been at least one order of magnitude smaller than the threshold for all the materials considered here. Therefore, mirrors with  $L_M = 50$  cm are able to handle the XFEL beam well under the threshold even for the bigger beam size at lower energies.

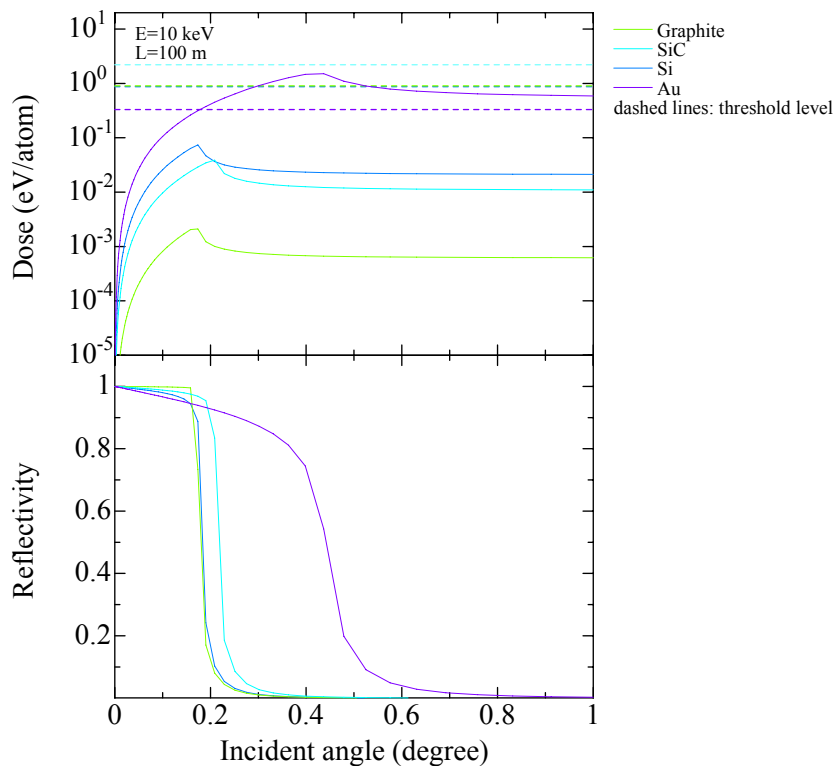


Fig. A1-4-1 Glancing angle dependence of the dose at  $E_p = 10$  keV

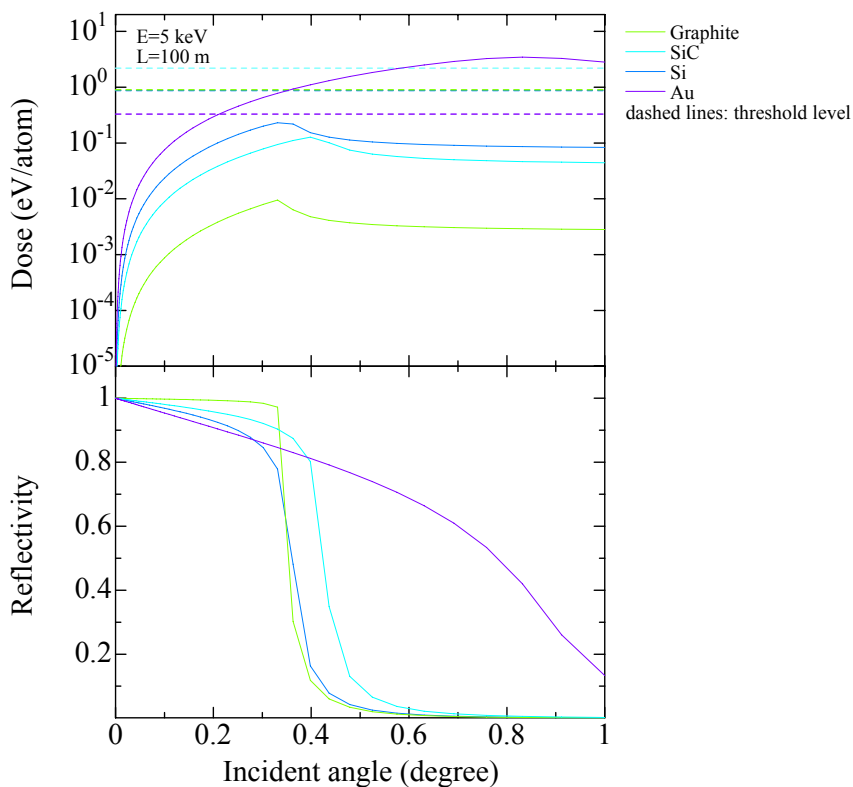


Fig. A1-4-2 Glancing angle dependence of the dose at  $E_p = 5$  keV

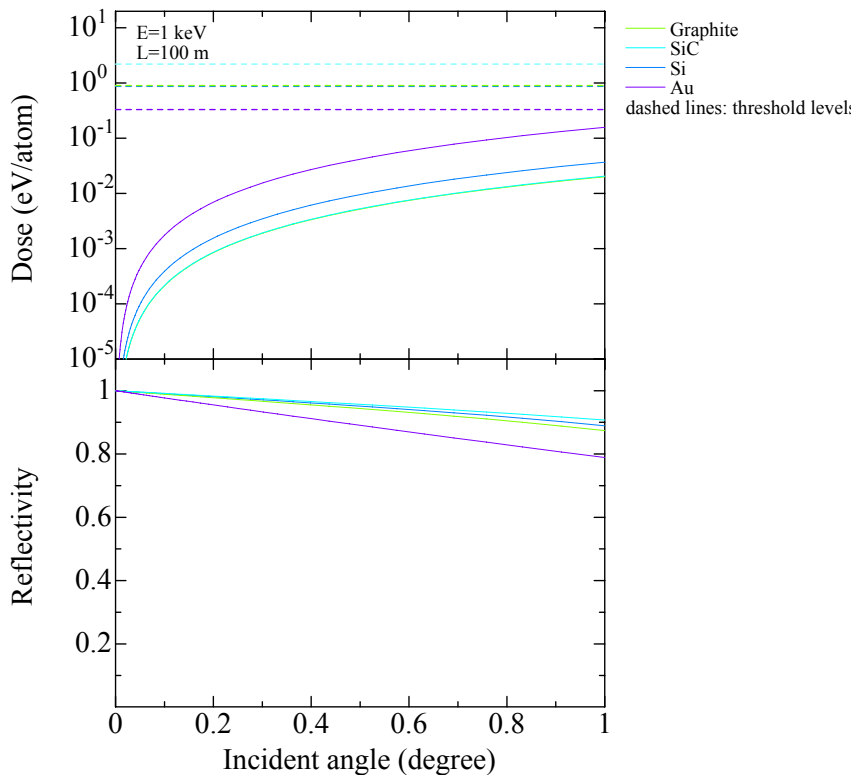


Fig. A1-4-3 Glancing angle dependence of the dose at  $E_p = 1 \text{ keV}$

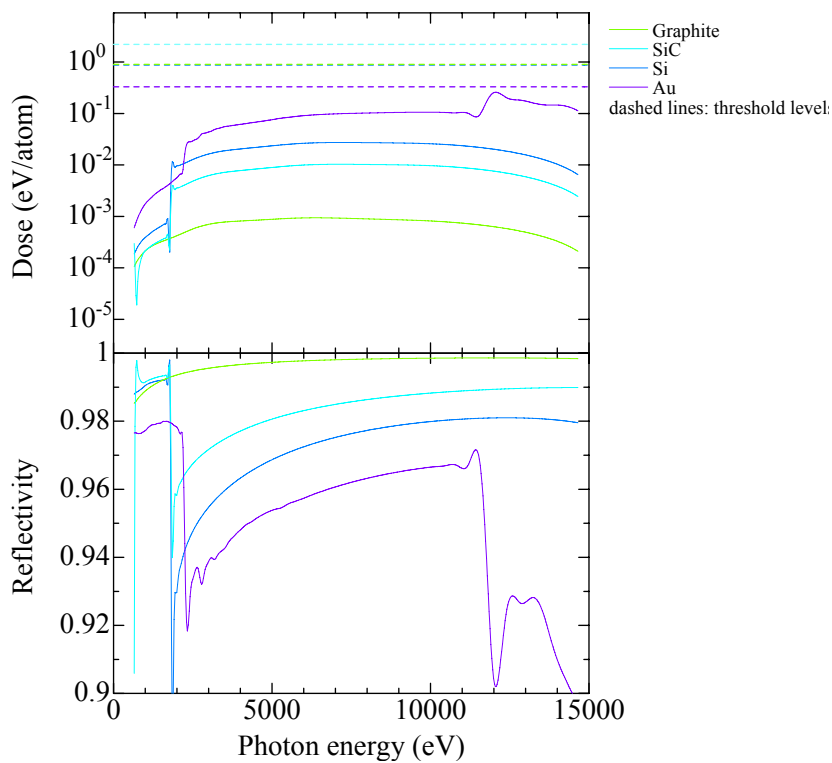


Fig. A1-4-4 Photon energy dependence of the dose at  $\theta = 0.1^\circ$

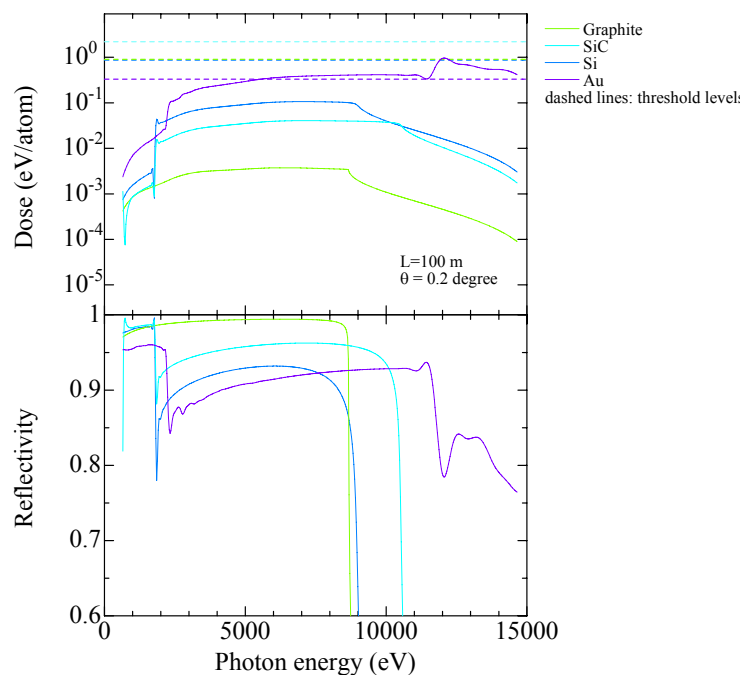


Fig. A1-4-5 Photon energy dependence of the dose at  $\theta = 0.2^\circ$

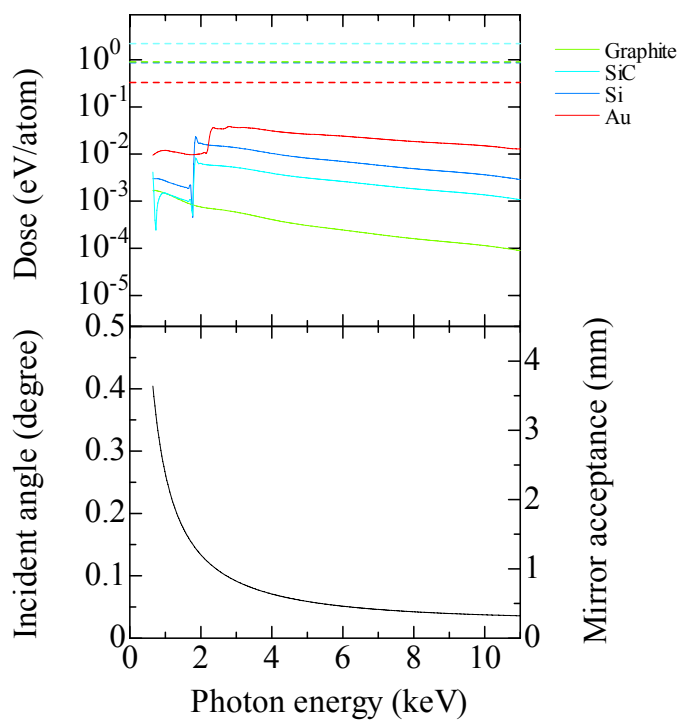


Fig. A1-4-6 The dose (above), glancing angle (below, left axis) and mirror acceptance (below, right axis) for a fixed mirror placed at  $L=100\text{ m}$  with a length of  $L_M = 50\text{ cm}$ , when the ratio of the acceptance and the beam size is fixed at 6 by changing the glancing angle.

## A1-5. Discussion

(1) A two-stage structure is necessary for the beam blocking optical component. The material directly irradiated by the XFEL beam should be made of a light element such as  $B_4C$  to prevent melting and/or evaporation. After attenuating the beam power sufficiently by this light material, the second-stage, heavier metal element blocks the hard X-rays and/or gamma rays.

(2) Be and diamonds can be used in all energy ranges for vacuum tight windows.

(3) A Si monochromator crystal can be safely used above 6 keV. A Diamond crystal works better for the lower energy region (3 ~ 6 keV) with respect to radiation doses.

(4) When a total reflection mirror is operated near the critical angle, lighter materials such as SiC and/or C are preferable. However, with a smaller glancing angle of  $\theta \leq 0.2^\circ$ , Si is a good candidate. The energy dependence of the beam size demands an adjustment to the glancing angle in order not to miss any part of the beam. A 50 cm mirror made of any material can capture the entire beam without any problems related to radiation doses.

The results are summarized in the following table (Table A1-5-1).

Table A1-5-1 Radiation tolerance of the optical components

	Classification	Material	Tolerance
(1)	Beam Blocking (Shutter/Collimator)	$B_4C$ , SiC, Be, Diamond	◎
		Cu	×
(2)	Vacuum windows	Be, Diamond	◎
(3)	Monochromator crystals	Si	○
		Diamond	◎
(4)	Total Reflection Mirrors	Au	△
		Si	○
		SiC	◎
		C	◎

## Reference:

R. Tatchyn, "LCLS optics: Technological issues and scientific opportunities," SLAC-PUB 6064, 1993.

R. M. Bionta, "Controlling doses to low Z solids at LCLS," LCLS note LCLS-TN-00-3, 2000.

M. Yabashi et al, "Optics development for the Japanese XFEL project", Proc. SPIE 6586, p. 658605.

## A2. Estimation of Transmissivity

### A2-1. Introduction

The transmissivities of some solid-state and gas-phase materials were estimated in order to discuss the specification of attenuators.

Transmissivities of X-rays for solid-state and gas-phase (@293K) materials consisting of a single atomic species are given by the following formula:

$$T = \exp\left(-3.394 \times 10^{13} \frac{\lambda(\text{m}) \rho(\text{g/cm}^3) f'' z(\text{cm})}{M(\text{g/mol})}\right), \quad (\text{Eq. A2-1-1})$$

and

$$T = \exp\left(-1.395 \times 10^4 \times \lambda(\text{m}) P(\text{Pa}) f'' z(\text{cm})\right), \quad (\text{Eq. A2-1-2})$$

where  $f''$  is the imaginary part of the atomic scattering factor,  $z$  the thickness of the attenuator,  $\rho$  the density,  $M$  the molar mass, and  $P$  the pressure.

## A2-2. Solid Attenuator

The following estimations were made for some solid state attenuators:

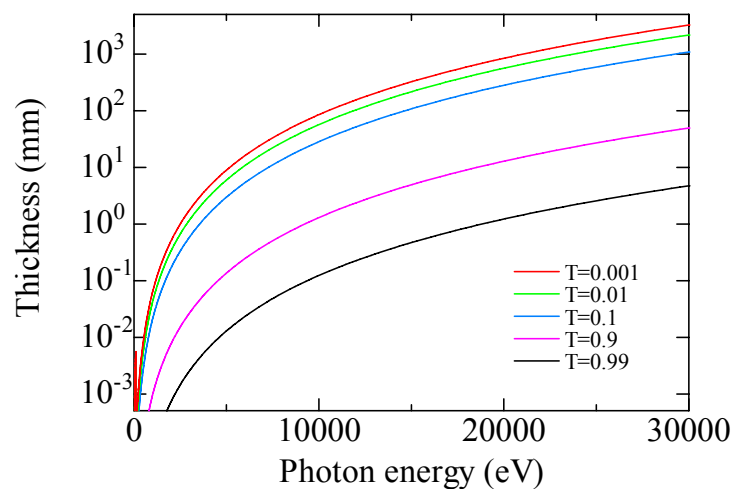
1. Energy dependence of the attenuator thickness for various transmissivity values,  $T$ .
2. Energy dependence of the transmissivity,  $T$ , for various attenuator thickness,  $z$ .

(1) Be

$$\rho = 1.85 \text{ g/cm}^3, M = 9.012 \text{ (g/mol)}$$

It can be used for attenuation of X-rays below 3 keV.

(a)



(b)

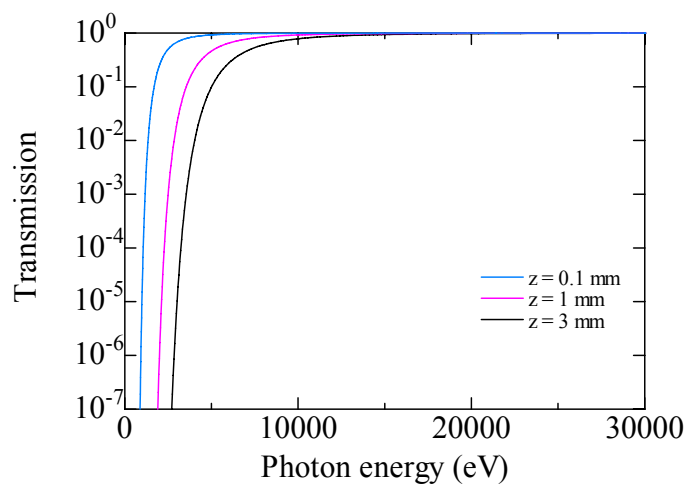
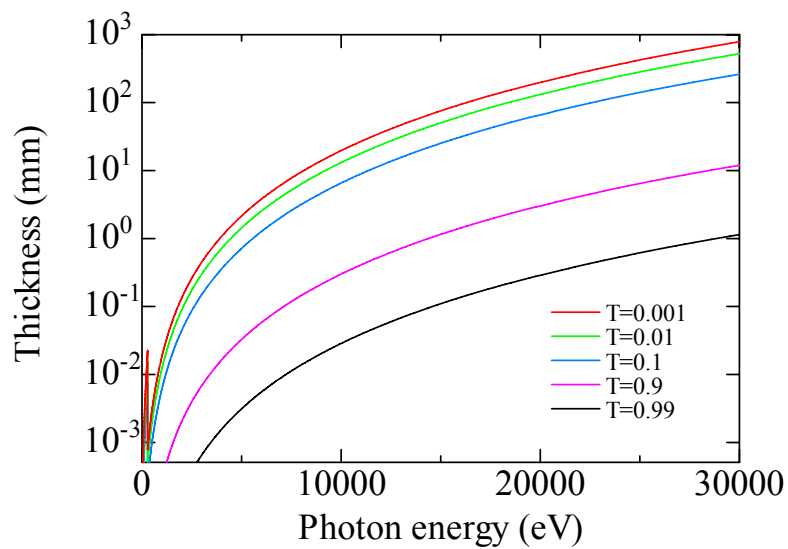


Fig. A2-2-1 X-Ray Transmissivity of Be.

## (2) Isotropic Carbon

 $\rho=1.7 \text{ g/cm}^3$ ,  $M = 12.0 \text{ (g/mol)}$  $10^{-2}$  attenuation at 15 keV need thickness of more than 60 mm.

(a)



(b)

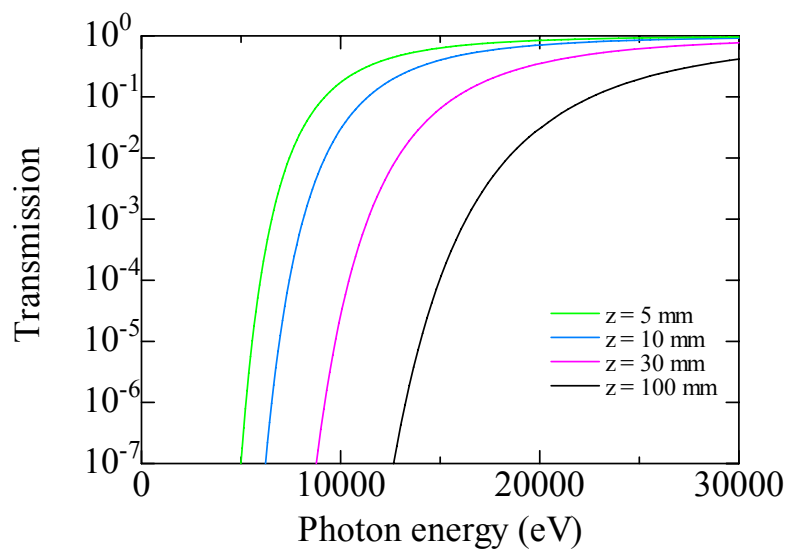


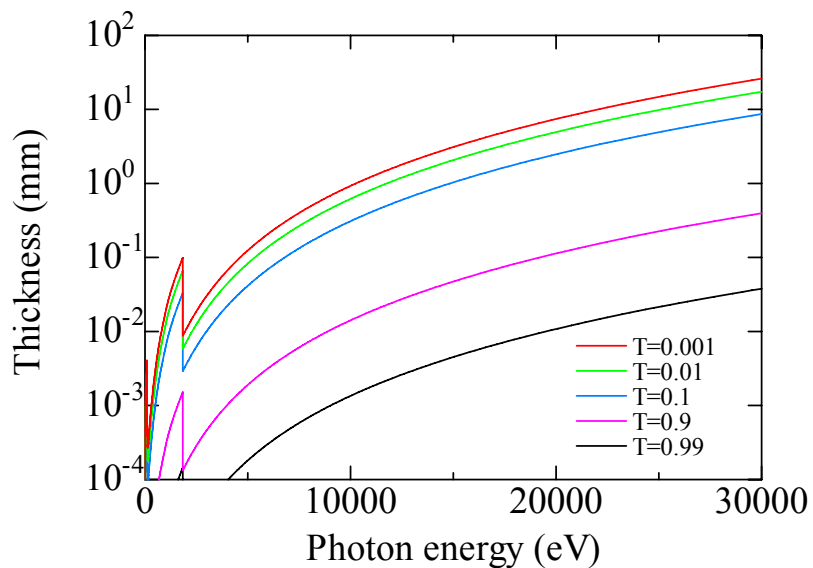
Fig. A2-2-2 X-Ray Transmissivity of Isotropic Carbon

(3) Si

 $\rho=2.33 \text{ g/cm}^3$ ,  $M = 28.1 \text{ (g/mol)}$ 

Transmissivity for 10 keV X-rays varies from 50% to 0.1% as the thickness varies from 100  $\mu\text{m}$  to 3 mm. The transmissivity at 7 keV and 100  $\mu\text{m}$  thick is 10%. A thinner attenuator is required to produce higher transmissivity. It is difficult to use for small attenuation at less than 5 keV.

(a)



(b)

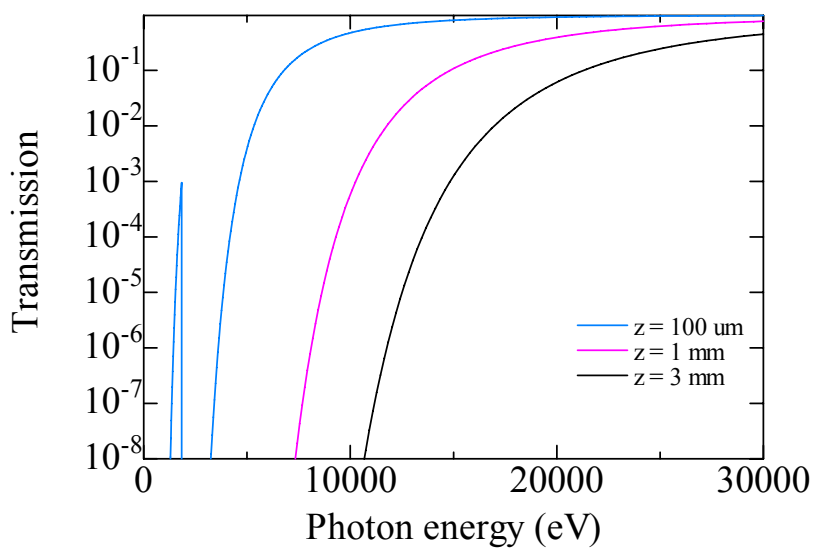


Fig. A2-2-3 X-Ray Transmissivity of Si

## A2-3. Gas Attenuator

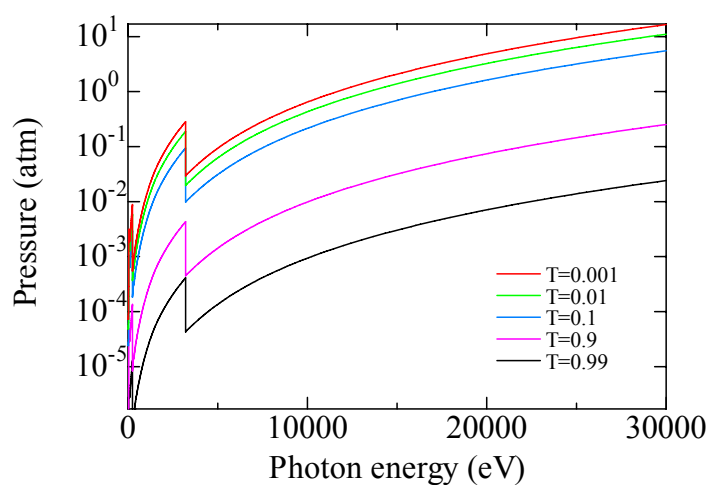
The following estimations were made for some gas phase attenuators with a fixed thickness of 1 m:

1. Energy dependence of the attenuator pressure,  $P$ , for various transmissivity values,  $T$ .
2. Energy dependence of the transmissivity,  $T$ , for various attenuator pressures,  $P$ .

(1) Ar,  $z=1$  m

A pressure range above 0.1 atm corresponds to the transmissivity from 100% to 10% at 7 keV. An extremely wide attenuation range is given between 3~5 keV.

(a)



(b)

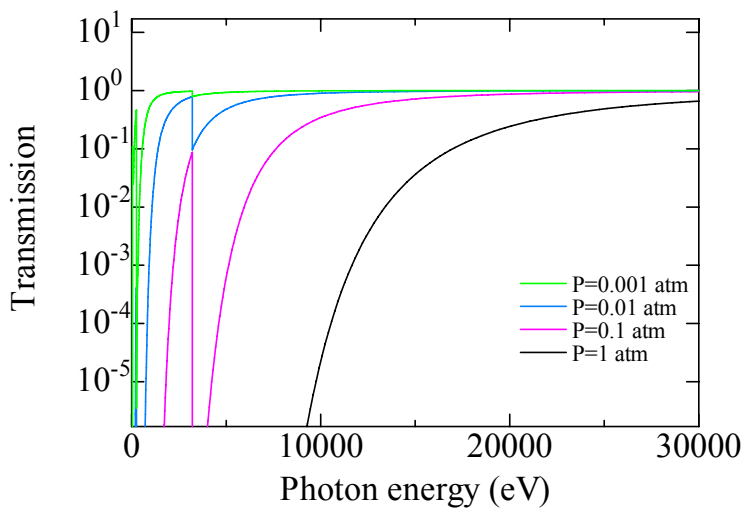
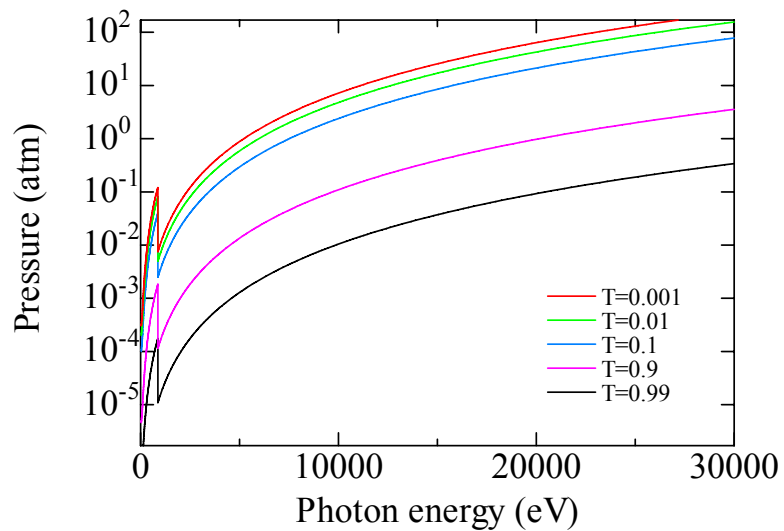


Fig. A2-3-1 X-Ray Transmissivity of Ar

(2)Ne,  $z=1$  m

A pressure range below 0.1 atm corresponds to the transmissivity from 100% to 3% at 3 keV.

(a)



(b)

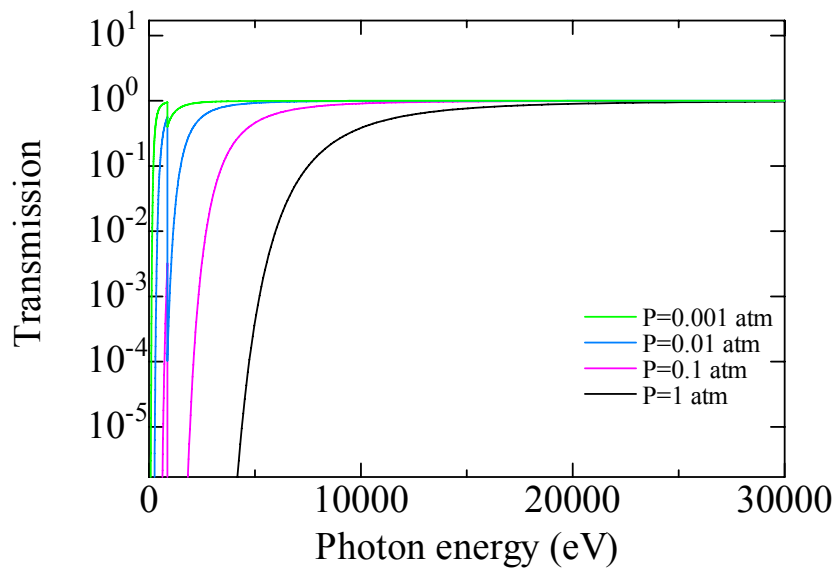
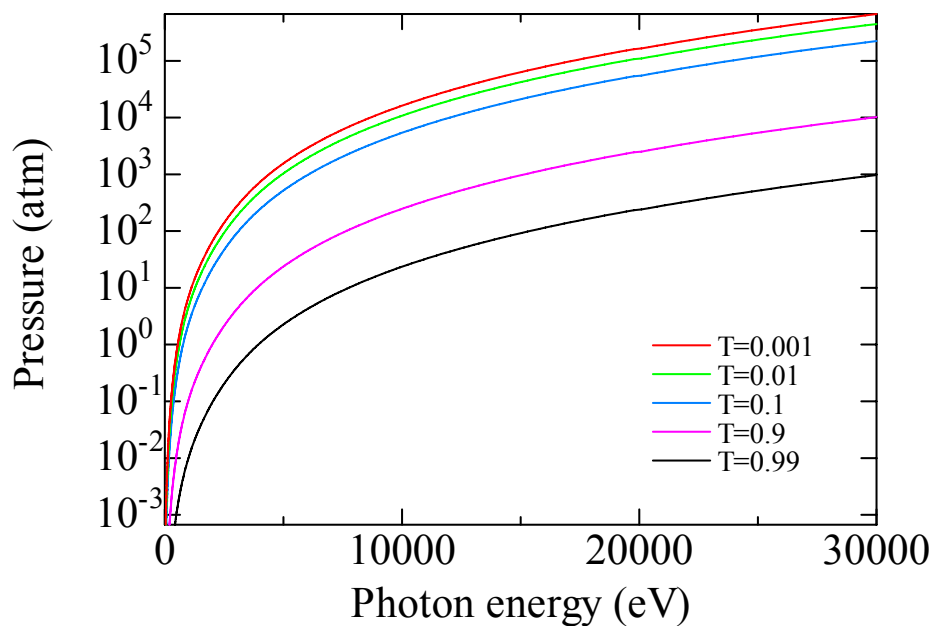


Fig. A2-3-2 X-Ray Transmissivity of Ne

(3)He, z=1 m

Absorption is negligible for &gt;1 keV photons when the pressure is less than 0.1 atm.

(a)



(b)

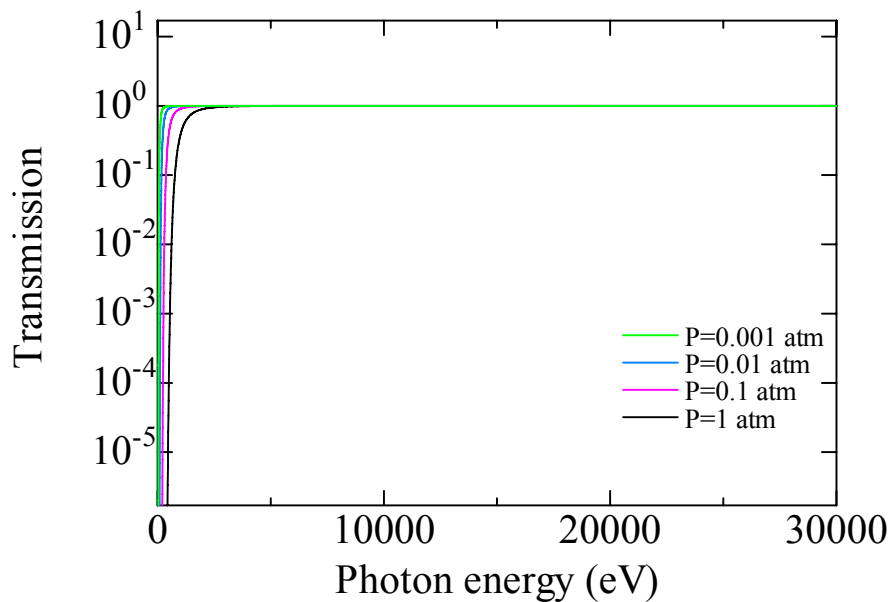


Fig. A2-3-3 X-Ray Transmissivity of He

## A2-4. Summary

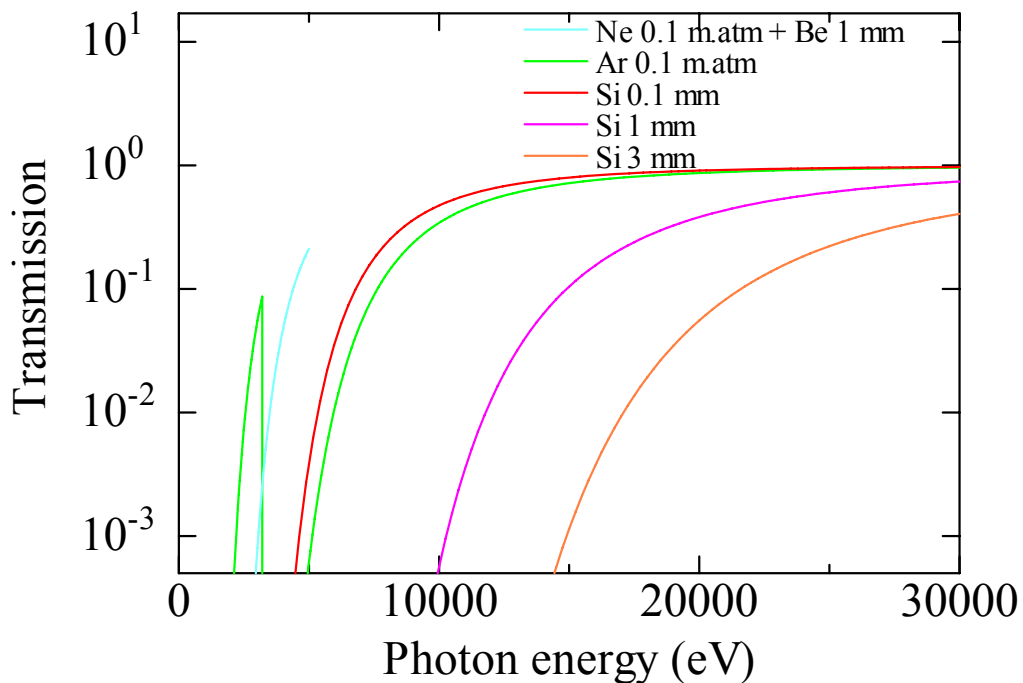


Fig. A2-4-1 X-ray transmissivity of various attenuators

A transmissivity control above 0.1% can be performed as follows:

- (1)  $h\nu < 3$  keV: combination of Ne ( $zP < 0.1$  m.atm) and Be ( $z < 1$  mm),
- (2)  $3 < h\nu < 5$  keV: Ar ( $zP < 0.1$  m.atm)
- (3)  $5 < h\nu < 10$  keV: combination of Ar ( $zP < 0.1$  m.atm) and Si ( $100 \mu\text{m} < z < 1$  mm).
- (4)  $10 < h\nu < 15$  keV: combination of Ar ( $zP < 0.1$  m.atm) with Si ( $100 \mu\text{m} < z < 3$  mm).

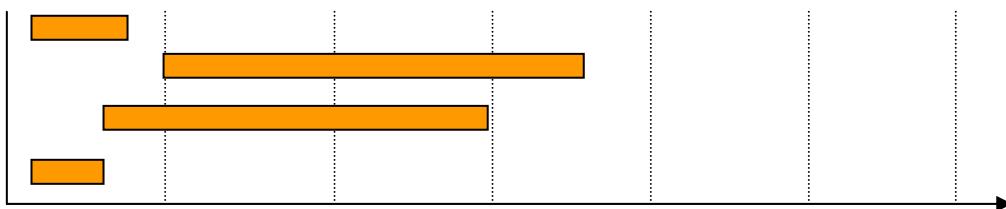


Fig. A2-4-2 Energy range covered with each attenuator

### A3. Estimation of Scattering Power

Scattered intensity of X-rays is given for monatomic solid state materials and gas phase materials at T=293K by the following equations:

(solid)

$$\begin{aligned}\frac{I_s (\text{phts/pls})}{I_0 (\text{phts/pls})} &= \frac{\rho (\text{g/cm}^3) N_A (1/\text{mol})}{M (\text{g/mol})} z (\text{cm}) r_e^2 (\text{cm}^2) [F(x)^2 + S(x)] P_g \Delta\Omega \\ &= 6.02 \times 10^{23} \times 7.94 \times 10^{-26} \times \frac{\rho (\text{g/cm}^3)}{M (\text{g/mol})} z (\text{cm}) [F(x)^2 + S(x)] P_g \Delta\Omega \\ &= 0.0478 \times \frac{\rho (\text{g/cm}^3)}{M (\text{g/mol})} z (\text{cm}) [F(x)^2 + S(x)] P_g \Delta\Omega\end{aligned}$$

(gas)

$$\begin{aligned}\frac{I_s (\text{phts/pls})}{I_0 (\text{phts/pls})} &= \frac{\rho (\text{g/cm}^3) N_A (1/\text{mol})}{M (\text{g/mol})} z (\text{cm}) r_e^2 (\text{cm}^2) [F(x)^2 + S(x)] P_g \Delta\Omega \\ &= 4.11 \times 10^{-10} \times 6.02 \times 10^{23} \times 7.94 \times 10^{-26} P (\text{Pa}) z (\text{cm}) [F(x)^2 + S(x)] P_g \Delta\Omega \\ &= 1.96 \times 10^{-11} P (\text{Pa}) z (\text{cm}) [F(x)^2 + S(x)] P_g \Delta\Omega\end{aligned}$$

ex1) Be:  $\rho=1.85 \text{ g/cm}^3$ ,  $M=9.012 \text{ (g/mol)}$ ,  $z=100 \text{ um}$ ,  $F(x)^2+S(x) \sim 4$ ,  $P_g \sim 1$ ,

$\Delta\Omega= 10 \times 10 \text{ mm}^2 / (30 \times 30 \text{ mm}^2) = 0.1 \text{ sr}$  (placing a detector with  $10 \times 10 \text{ mm}^2$  detecting area 30 mm from the scatterer)

$$\frac{I_s (\text{ph/pls})}{I_0 (\text{ph/pls})} \cong 0.0478 \times \frac{1.85}{9.01} \times 0.01 \times 4 \times 0.1 = 4 \times 10^{-5}$$

ex2) Ar:  $P=0.1 \text{ atm}$ ,  $z=10 \text{ cm}$ ,  $F(x)^2+S(x) \sim 10$ ,  $P_g \sim 1$ ,

$\Delta\Omega = 30 \times 30 \text{ mm}^2 / (50 \times 50 \text{ mm}^2) = 0.3 \text{ sr}$  (placing a detector with  $\square 30 \text{ mm}^2$  detecting area 50 mm from the scatterer)

$$\frac{I_s (\text{ph/pls})}{I_0 (\text{ph/pls})} \cong 1.96 \times 10^{-11} \times 1.02 \times 10^4 \times 10 \times 10 \times 0.3 = 6 \times 10^{-6}$$

ex3) He:  $P=0.1 \text{ atm}$ ,  $z=10 \text{ cm}$ ,  $F(x)^2+S(x) \sim 2$ ,  $P_g \sim 1$ ,

$\Delta\Omega = 30 \times 30 \text{ mm}^2 / (50 \times 50 \text{ mm}^2) = 0.3 \text{ sr}$  (placing a detector with a detecting area of  $30 \text{ mm}^2$  at a distance of 50 mm from the scatterer)

$$\frac{I_s (\text{ph/pls})}{I_0 (\text{ph/pls})} \cong 1.96 \times 10^{-11} \times 1.02 \times 10^4 \times 2 \times 10 \times 0.3 = 1.2 \times 10^{-6}$$

Reference:

S. Goto, Thesis, Univ. Tokyo (2000).

#### **A4. Revision Record**

1st version in Japanese: 17 June 2008

1st version in English: February 2010